PERFORMANCE ENHANCEMENT OF FIELD ORIENTED INDUCTION MOTOR DRIVE SYSTEM

by

Adil Khurram

A Thesis Presented to the Faculty of the
American University of Sharjah
College of Engineering
in Partial Fulfillment
of the Requirements
for the Degree of

Master of Science in
Electrical Engineering

Sharjah, United Arab Emirates

November 2016

Approval Signatures

We, the undersigned, approve the Master's Thesis of Adil Khurram.

Thesis Title: Performance Enhancement of Field Oriented Induction Motor Drive System

Signature	**Date of Signature** (dd/mm/yyyy)
_____	_____
Dr. Habibur Rehman Associate Professor, Department of Electrical Engineering Thesis Advisor	
_____	_____
Dr. Shayok Mukhopadhyay Assistant Professor, Department of Electrical Engineering Thesis Advisor	
_____	_____
Dr. Rached Bin H'mida Dhaouadi Professor, Department of Electrical Engineering Thesis Committee Member	
_____	_____
Dr. Mamoun Fahed Saleh Abdel-Hafez Associate Professor, Department of Mechanical Engineering Thesis Committee Member	
_____	_____
Dr. Nasser Qaddoumi Head, Department of Electrical Engineering	
_____	_____
Dr. Mohamed El-Tarhuni Associate Dean, College of Engineering	
_____	_____
Dr. Richard T. Schoephoerster Dean, College of Engineering	
_____	_____
Dr. Khaled Assaleh Interim Vice Provost for Research and Graduate Studies	

Acknowledgements

It is a genuine pleasure to express my deep gratitude and thanks to my parents for encouraging me to continue higher education. I am forever in debt to them for their continuous support during this journey. I would like to thank my thesis advisors, Dr. Habibur Rehman and Dr. Shayok Mukhopadhyay for their guidance and support to make this thesis successful. Furthermore, I would also like to thank the Department of Electrical Engineering at American University of Sharjah for granting me the graduate assistantship that enabled me complete my Masters' studies.

I would like to express gratitude to my friend and colleague Mr. Daniyal Ali for his assistance during the course of the thesis work.

A sincere thanks to my friends and colleagues Seyed, Ahlam, Andrew, Aly, Ameen, Hesham for making my stay at AUS memorable.

Dedicated to my family . . .

Abstract

This research focuses on the performance enhancement of an indirect field oriented (IFO) induction motor drive system by designing an efficient controller for speed regulation and by maintaining optimal operation of a three phase inverter. The most widely used techniques for three phase inverter operation are the space vector pulse width modulation, the sine triangle pulse width modulation (SPWM) and square wave mode of operation. The first objective of this research work is to design a synchronous SPWM technique with minimal total harmonics distortion (THD). SPWM performs better at low speed due to lower harmonics in the frequency spectrum, while square wave mode is beneficial at high speed operation because of its higher DC bus utilization. The inverter mode of operation is switched from SPWM to square wave when the motor operates above the base speed for higher DC bus utilization. The sudden inverter mode switching results in unwanted torque ripples and therefore degrades the speed controller performance. Thus the second objective of this work is to design a mode switching strategy which ensures a torque ripple free transition. The speed regulator performance enhancement is the third main objective of this work. Conventionally, a linear integer order proportional integral (IO-PI) controller regulates the motor speed. However, the fractional order proportional integral (FO-PI) controllers have been documented to perform better than IO-PI controllers due to their Iso-damping property. Therefore, in this work the performance of a nonlinear FO-PI controller is compared with integer order controllers such as Ziegler-Nichols proportional integral (ZN-PI) controller, Cohen-Coon proportional integral (CC-PI) controller and a proportional integral controller tuned via trial and error (TE-PI) method are designed. Simulation and experimental investigation proves that FO-PI controller has better speed tracking, less settling time, exhibits better disturbance rejection and low speed tracking and can even control a detuned motor's speed very well.

Search Terms: ***Induction Motor, Field Oriented Control, Synchronous SPWM, Fractional Order PI Controller, Non-linear Controller***

Table of Contents

List of Figures

List of Tables

Chapter 1: Introduction and Literature Review

AC motors are being deployed in the industry in a large number of applications such as electric vehicles, traction motors, automation and process industry etc. These machines are preferred over Direct Current (DC) motors because of their rugged structure and compact size [1]. Moreover, these machines are less sensitive to the environment. The high performance control of such motors is possible through the entire speed range via variable frequency inverters or stator or air gap flux oriented vector controlled schemes. Variable speed drives that employ both square-wave and Pulse Width Modulated (PWM) inverters are also used in the industry [2] specifically, for high power applications.

The two most promising machines i.e. Induction Motors (IM) and Permanent Magnet Synchronous Motors (PMSM) are being investigated by the automotive industry for various Alternate Energy Vehicle (AEV) applications [3–7]. Ford's Focus, Toyota's Prius, Chevy's Volt and Nissan's Leaf [4] are some of the electric vehicles that use PMSM while Tesla's Roadster, Tesla's Model S, Ford's P2000 [5], and Hyundai's ix35 Fuel Cell Vehicle (FCV) [6] as well as the US army's heavy duty HEVs [4] have opted for an induction motor. The incentive to opt for an induction motor (IM) is attributed to its low cost and rugged nature. Although the PMSM has higher efficiency than the induction machine, it suffers from the problems of demagnetization over time and also requires rare earth elements that make it expensive. Therefore, this work focuses on an induction motor based drive system for the AEV traction application.

The theory of field oriented control, first proposed by Blaschke and Hasse [8], laid the foundation for the high performance control of induction motors which is similar to the decoupled control of flux and torque of DC motors. The basic idea behind the field oriented control is to control an induction motor like a separately excited DC motor [9]. Field Oriented Control (FOC) is usually divided into Indirect Field Oriented Control (IFOC) and Direct Field Oriented Control (DFOC) [9]. IFOC scheme is a preferable choice compared to DFOC and Direct Torque Control (DTC) [10]. This scheme is only sensitive to the rotor time constant (T_r). In contrast to indirect field orientated scheme, the direct field oriented scheme uses the motor flux information which

is either measured or estimated. Different techniques to measure the flux have been proposed in [11–13]. But flux measurement is not always suitable and flux estimation schemes such as [14–17] are always preferred. However, the flux estimation is sensitive to almost all the parameters of the machine. The DTC on the other hand has been documented to have high torque ripples.

Indirect field orientation and direct field orientation schemes are usually implemented in rotor reference frame. The same techniques can be also implemented in stator reference frames as well as in air gap flux reference frames. Based on this idea, authors in [18] developed a universal field oriented controller that can incorporate IFO and DFO in any frame of reference. They also showed that use of reference frames other than the rotor reference frame enables DFO scheme to eliminate all steady state detuning effects. The work presented in this thesis will focus on a rotor flux oriented IFO drive system as the main test bench.

Three phase inverter fed induction motor drives are usually operated using Sine Triangle Pulse Width Modulation (SPWM) and Space Vector Pulse Width Modulation (SV-PWM) techniques. However, an induction motor drive operating under square wave or six step mode provides the benefits of higher DC bus utilization and lower switching losses as compared to other modes of operation. Therefore, for high power, high speed operation i.e. above base speed, square wave inverter is preferred. Furthermore, the efficiency of the system is high when square wave inverters are used above the base speed and during low output power conditions [2, 19–21]. However, harmonics in the currents and voltages of six-step inverter lie very close to fundamental frequency of the motor and thus, require expensive filters to remove these unwanted harmonics. This harmonics problem is more dominant at low speed. A drive system that can benefit from both modes of operations, effectively increases the drive system performance.

The presence of low order harmonics increases the machine losses in the drive system and adversely affects the efficiency especially at low speed. The effect is more pronounced at low speed because, at low speed, the motor leakage reactance due to low order harmonics is low. Therefore, motor draws high current due to low order harmonics that results in higher core losses in the machine. This effect of leakage reactance is considerably lower at high speed where the higher operating frequency increases the

leakage reactance due to relatively higher frequency of low order harmonics thus decreasing the harmonic current. The efficiency of the machine is reduced to a large extent due to this lower reactance of the machine at lower speed [2]. Therefore, a square wave inverter with low order harmonics is not a favorable choice at low speed but has lesser adverse effects at higher motor speed. The operation of induction motor drives above the base speed requires higher voltage to achieve higher speed in industrial applications. SPWM technique is limited by lower DC bus utilization and become impractical when the fundamental frequency at which the motor operates becomes very high. Thus, for the motor operation above the base speed square wave inverters can be employed. This work focuses on SPWM and square wave modes of operations. SPWM reduces the harmonic content in the motor current and voltage by shifting the harmonics at multiples of carrier frequency. Moreover, the starting performance of SPWM based induction motor drive is better than the square wave operated drive system [20]. But the drawback of this scheme is that it can produce higher switching losses when operating in high power, high speed applications. The solution is to overcome the short comings of both of these schemes and employ different schemes under different conditions.

The idea of taking advantage of both schemes has been explored for various applications. Both the SPWM and square wave mode of operation are incorporated together to benefit from their advantages in [20, 21] at different operating speed and load conditions. The inverter mode is therefore switched from SPWM to square wave while the motor speed increases above the base speed and vice versa. Torque ripples are produced if the mode switching from sine triangle to square wave is not properly realized [22]. Authors of [20] proposed to switch the mode when one of the three phase currents is zero to ensure constant output power during transition. A seamless transition has been realized in [21] for a V/f drive system by forcing the carrier to zero. This work extends the technique proposed for V/f control to a field oriented drive system.

Higher switching frequency of the inverter introduces harmonics which can be suppressed to a large extent by the inertia and low inductance of the machine acting as a low pass filter [23, 24]. Moreover, the presence of harmonics introduces torque ripples, increases the harmonic current [25] and can be reduced by synchronous pulse width modulation (PWM) [26]. Synchronization between the fundamental frequency

and carrier frequency (3-φ, halfwave, quarter-wave symmetry) essentially removes the sub-harmonics especially at low speeds [27]. A sub-harmonic elimination technique using synchronized PWM for SV-PWM was proposed in [28] and compared with the conventional synchronization technique. Moreover, the electromagnetic interference (EMI) produced due to high switching frequency of the inverter is studied and consequently a spread spectrum technique was developed in [29] to reduce the EMI emissions.

Maintaining a linear relationship between the fundamental and carrier frequency has been discussed in the literature to maintain synchronism [27]. The carrier frequency is kept at an odd integer multiple (m) of the fundamental operating frequency. An upper bound is usually defined on the carrier frequency based on the maximum allowable switching frequency (f_{max}) and is derived from the operating limits of the inverter. At high speed, the carrier frequency approaches the maximum allowable limit (f_{max}). Therefore, when the switching frequency approaches this maximum allowable limit (f_{max}), this multiple 'm' is decreased dynamically. This reduction in the multiple of carrier frequency can lead to sudden changes in the carrier frequency. During steady state operation, a sudden change in the carrier frequency can lead to disruption in the speed tracking.

Motor losses are inversely proportional to the switching frequency. Increasing the switching frequency decreases the motor losses [29] but at the same time increases the inverter switching losses. These inverter losses in the semiconductor devices increase in direct proportion to the switching frequency or carrier frequency. Therefore, optimum carrier frequency operation is proposed in [29]. The design of PWM inverters should consider the inverter switching losses at high carrier frequency and motor losses at low switching frequency (f_c) during variable speed operation. At low speeds, f_c should be low to decrease the inverter switching losses while at the same time high enough to reduce motor losses. On the contrary, f_c should be large at high speeds to lower motor losses because motor losses are greater than inverter losses at high speeds. Inverter carrier frequency should be adjusted to minimize both of these losses.

A linear relationship between the fundamental and carrier frequency can no longer ensure this kind of operation due to the fact that motor losses depend upon the construction of the iron core and no exact relationship exists to calculate these

losses [29]. Therefore, this work attempts to design a quadratic function based on the analysis of the harmonic efficiency data collected at various speeds and carrier frequencies. Also, it proposes a smooth mode transition technique from SPWM inverter to square wave mode when the motor moves from low to high speed operation and vice versa.

The second part of this thesis focuses on the design of speed regulator for an indirect field oriented induction motor drive system. A motor controller plays a vital role in the dynamic performance as well as steady state performance of Alternate Energy Vehicles, and numerous other automation and process control applications. An accurate, rapid and robust speed controller design is critical for high performance induction motor drive system. The two main types of controllers that are being implemented for torque/speed control of various machines are: (1) Linear proportional integral (PI) controllers and (2) Nonlinear controllers. Fractional order controllers are nonlinear controllers that have the potential to perform better than linear controllers.

The application of fractional calculus to the control theory has led to the development of fractional order proportional integral (FO-PI) controllers. FO-PI controller is similar to the integer order proportional integral controller (IO-PI). However, the FO-PI controller differs from the IO-PI controller in the sense that instead of using an integral of integer order, a fractional order integral is used.

Fractional calculus can be also used to obtain the fractional order model of the plant. Therefore, fractional order controllers can be used for both cases i.e. integer order (IO) plant model and fractional order (FO) plant model. The reverse is also possible i.e. integer order controller can be used for fractional order plant. Since most of the systems have already been established as IO models, therefore, the most common scenario is the use of FO controllers for IO plants [30]. It is useful to consider the design of an FO controller for an integer order plant [31] to enhance the system performance.

An integer order PI controller still dominates the industry because of its simplicity and ease of implementation. The industry remains reluctant to shift towards complex nonlinear controllers for an incremental increase in the drive system performance. Traditionally, PI controllers were designed using trail and error tuning procedure. However, tuning rules have also been proposed for designing linear PI controller. The rules

provided by Ziegler-Nichols [32] have been widely accepted and adopted in industrial applications. Moreover, several variations of existing tuning rules for linear PI controllers have also been proposed in the literature. One such modification is proposed by Cohen-Coon [33].

Though linear PI controllers are widely used by the industry, their performance degrades due to inherent fundamental limitations like saturation and reduced stability margin etc. [34]. The performance of linear PI controller degrades when it is used for a nonlinear plant like an induction machine. Moreover, the variation in motor parameters causes further deterioration of PI controller performance, and it has a long recovery time when subjected to external disturbances. Here by recovery time we mean the time required for the motor speed to return to a given set-point value. The induction motor and permanent magnet synchronous motor (PMSM) are nonlinear plants, and are expected to perform better when using a nonlinear controller as compared to linear controllers. Therefore, nonlinear controllers are being investigated [34–50] for these types of motors.

Recently, auto disturbance rejection controllers (ADRCs) are being explored because of their ability to estimate and compensate for external disturbance without exact knowledge of the plant parameters [35, 36]. ADRC employs generalized derivatives and generalized functions based extended state observer (ESO) to estimate disturbance, thus is further dependent upon certain generalized parameters [35]. However, incorrect selection of ADRCs parameters can lead to divergence of disturbance estimator. Moreover, the use of second and third order ADRC with third order dynamic equations for ESO leads to high computational cost [36]. Hamiltonian based [37] and passivity based [38] nonlinear controllers are investigated for improving the performance of induction motor drive system. These controllers [35] are also dependent upon the system parameters. Back-stepping, adaptive back-stepping, and extended state observers have been proposed to compensate for the controller parameters variation [35].

Nonlinear model predictive control (NMPC) schemes [39]- [42] adjust the control input based on the time evolution of the system model. NMPC is system model dependent because it evaluates beforehand, the control signal to be applied to the motor in order to track a known future reference. However, this controller is computation-

ally intensive because model predictive control [50] requires the solution of an optimal control problem at each sampling instant, which further increases the computational cost.

Sliding mode control is robust to parameters variation and shows a fast dynamic response [43] which makes this controller an attractive choice for the electric drives applications [43]- [46]. However, the sliding mode controller, when used for speed regulation [45,46] introduces chattering which causes torque ripples in an AC machine. Adaptive fuzzy sliding mode controllers have been used to avoid the chattering problem [46]. Fuzzy-logic controllers provide a systematic way to incorporate the expertise of the control engineer into the controller which makes it more robust and gives better performance even under certain parameters variation as compared to PI controller [47]- [49]. However, such approaches are dependent upon the skill of the engineer estimating the effect of a disturbance on plant output.

The nonlinear ADRC [34]- [36] are sensitive to the controller parameters, NMPC [39]- [42] is computational intensive, sliding mode [43]- [46] though is a robust controller but suffers from the chattering problem which induces torque ripples. Fuzzy logic controller [47]- [49] performs better than integer order PI controller yet requires rigorous tuning and is computationally intensive. Therefore, this work proposes a nonlinear FO-PI controller for the speed control of an induction motor drive system. The proposed controller has potential to perform better than linear PI controllers and when compared to other nonlinear controllers [34–50], is simpler to implement and is less motor parameters dependent.

1.1. Contributions

This research focuses on the performance enhancement of the field oriented induction motor drive system performance on both fronts of the three phase inverter control and the speed regulator. The square wave and SPWM as the two main techniques of inverter control and operation are discussed and implemented. The drawbacks and benefits of each technique are demonstrated and their performance is compared. A novel technique is developed to take advantage of each of these methods. The second focus of

this research work is to investigate the existing speed control algorithms and design an efficient controller. Fractional order proportional integral controller has been selected to enhance the performance of speed regulator. Simulations followed by hardware implementation are used to demonstrate the control techniques developed during the course of this work. Following are the three major contributions made by this research work.

- This work collects the motor current data at various operating speeds with different carrier frequencies. The data is then analyzed offline for optimal carrier frequency selection. The optimal carrier frequency data results into a second degree polynomial which when incorporated in the motor controller proved to give an overall lesser THD compared to simple linear carrier frequency controller. The carrier frequency in both cases increases to the maximum allowable inverter switching frequency of 10 KHz at the base speed.
- The inverter is switched from SPWM to square wave mode above the base speed to attain higher DC bus utilization. This work proposes a seamless transition between SPWM and square wave mode by suppressing the carrier frequency to zero. The proposed strategy overcomes the problem of torque ripple observed and sluggish speed response seen in case of inverter conventional mode switching from sine triangle to square wave mode and vice versa.
- For the speed regulator design, this thesis makes three main contributions: (i) As per the knowledge of the author, for the first time, it investigates the potential of the nonlinear FO-PI controller for an induction motor drive system through simulation and experimental study and compares its performance with the conventional integer order PI controller. (ii) A simple procedure for gain tuning of the FO-PI controller based on the tuning rules provided in [30] is designed for the induction motor speed controller. (iii) Also for the first time it is shown that that an FO-PI controller can control even a detuned motor's speed very well and also maximizes the torque per amperes output of the induction machine.

1.2. Thesis Organization

In chapter two, basic concepts of field oriented control and simulation as well as implementation of an indirect field oriented induction motor drive system are presented. The proposed carrier frequency control of the three phase inverter is presented in chapter three along with the simulation and experimental results. Chapter four illustrated the design, simulations and experimental validation of the proposed Fractional Order Proportional Integral Controller (FO-PI) and compares its performance to other well known controllers. Finally, chapter five concludes the thesis and lists some of the possible future works.

Chapter 2: Field Oriented Control

The field oriented control (FOC) or vector control can be realized by the transformation of the dynamic equations of induction motor from three phase stationary frame of reference to a two phase synchronously rotating reference frame. This kind of transformation forces the induction motor to mimic the behavior of a DC motor. The field orientation or flux orientation can be either rotor flux oriented or stator flux oriented. Rotor flux orientation is selected for this research work to achieve decoupled control of flux and torque. High performance induction machine drives require fast torque/speed response which can be achieved by the field orientation.

The generalized model of an induction machine in the two phase stationary frame of reference is used to obtain the stator currents and fluxes interms of stator voltages (Eq. 1, 2) where η is the reciprocal of rotor time contant ($\frac{1}{T_r}$). The θ_e required for stator flux oriented DFO is calculated from estimated flux using Eq. 3, 4. The rotor flux can be estimated from the stator currents in two phase stationary reference frame as given by the mathematical expressions in Eq. 5, 6. The corresponding θ_e can then be calculated from Eq. 7 and 8 resulting in rotor flux oriented DFO drive.

$$\begin{bmatrix} pI_{\alpha s} \\ pI_{\beta s} \end{bmatrix} = \frac{1}{\sigma L_s} \begin{bmatrix} p\lambda_{\alpha s} \\ p\lambda_{\beta s} \end{bmatrix} + \frac{1}{\sigma L_s} \times \begin{bmatrix} \eta & \omega_r \\ -\omega_r & \eta \end{bmatrix} \begin{bmatrix} \lambda_{\alpha s} \\ \lambda_{\beta s} \end{bmatrix} + \begin{bmatrix} -\frac{\eta}{\sigma} & -\omega_r \\ \omega_r & -\frac{\eta}{\sigma} \end{bmatrix} \begin{bmatrix} I_{\alpha s} \\ I_{\beta s} \end{bmatrix} \tag{1}$$

$$\begin{bmatrix} p\lambda_{\alpha s} \\ p\lambda_{\beta s} \end{bmatrix} = \left(\begin{bmatrix} V_{\alpha s} \\ V_{\beta s} \end{bmatrix} - R_s \begin{bmatrix} I_{\alpha s} \\ I_{\beta s} \end{bmatrix} \right) \tag{2}$$

$$\lambda_s = \sqrt{\lambda_{\alpha s}^2 + \lambda_{\beta s}^2} \tag{3}$$

$$\theta_e = tan^{-1} \left(\frac{\lambda_{\beta s}}{\lambda_{\alpha s}} \right) \tag{4}$$

$$\begin{bmatrix} pI_{\alpha r} \\ pI_{\beta r} \end{bmatrix} = \frac{L_m}{\sigma L_s L_r} \begin{bmatrix} p\lambda_{\alpha r} \\ p\lambda_{\beta r} \end{bmatrix} - \frac{R_s}{\sigma L_s} \begin{bmatrix} I_{\alpha s} \\ I_{\beta s} \end{bmatrix} + \frac{1}{\sigma L_s} \begin{bmatrix} V_{\alpha s} \\ V_{\beta s} \end{bmatrix} \tag{5}$$

$$\begin{bmatrix} p\lambda_{\alpha r} \\ p\lambda_{\beta r} \end{bmatrix} = -\left(\begin{bmatrix} \eta & \omega_r \\ -\omega_r & \eta \end{bmatrix} \begin{bmatrix} \lambda_{\alpha r} \\ \lambda_{\beta r} \end{bmatrix} - \eta L_m \begin{bmatrix} I_{\alpha r} \\ I_{\beta r} \end{bmatrix} \right) \tag{6}$$

$$\lambda_r = \sqrt{\lambda_{\alpha r}^2 + \lambda_{\beta r}^2} \tag{7}$$

$$\theta_e = tan^{-1}\left(\frac{\lambda_{\beta r}}{\lambda_{\alpha r}}\right) \tag{8}$$

2.1. Field Orientation Principle

The theory of field oriented control outlines the procedure to obtain decoupled control of electromagnetic torque and flux. The principle of rotor field orientation is that entire rotor flux given by Eq. 7 and 8 is oriented along direct axis (*d-axis*) of the synchronously rotating reference frame and the rotor flux along quadrature axis (*q-axis*) is zero. The electromagnetic torque (T_e) in the two phase synchronously rotating frame of reference is given by Eq. 9. If the flux along *q-axis* is zero than the entire rotor flux will be aligned along *d-axis*. Eliminating the *q-axis* rotor flux component from the torque equation, results in Eq. 10 that depends only on i_{qs} and λ_{dr}. Realizing that under field orientation, the rotor flux λ_{dr} in the steady state condition is equal to the product of i_{qs} and L_m, therefore, we can re-write the torque in Eq. 10 as a product of i_{qs}, i_{ds} and constant $\frac{3PL_m^2}{2L_r}$ (Eq. 11). This leads us to the fact that the current along *d-axis* will control the flux and the current along *q-axis* will independently control the torque.

$$T_e = \frac{3P}{2}\frac{L_m}{L_r}\left(\lambda_{dr} i_{qs} - \lambda_{qr} i_{ds}\right) \tag{9}$$

$$T_e = \frac{3P}{2}\frac{L_m}{L_r}\left(\lambda_{dr} i_{qs}\right) \tag{10}$$

$$T_e = \frac{3P}{2}\frac{L_m^2}{L_r} i_{ds} i_{qs} \tag{11}$$

A set of three phase fluxes are produced in the rotor and the stator as a result of three phase set of voltages applied to the stator. The three phase flux in the rotor can be converted from stationary to two phase *dq-reference* frame. When the speed of rotation of the synchronous reference frame is set equal to the speed of rotation of the flux vector, than the resultant rotor flux is automatically aligned along the *d-axis* and the flux along *q-axis* is zero. The resultant rotor flux, aligned along the *d-axis*, makes an angle θ_e with the *a-axis* of the stationary frame fixed in the stator. In field orientation, the problem is the determination of θ_e which ensures that *d-axis* is locked with the rotor flux vector. The transformation matrices T, T^{-1}, $T_{\alpha\beta\rightarrow abc}$ and $T_{ab\rightarrow\alpha\beta}$ in Fig. 1, 2 required for conversion between different frames are given in Eq. 12 and Eq. 13 [51].

$$T_{\alpha\beta\rightarrow abc} = \begin{bmatrix} 1 & 0 \\ -\frac{1}{2} & \frac{\sqrt{3}}{2} \\ -\frac{1}{2} & -\frac{\sqrt{3}}{2} \end{bmatrix}, T_{ab\rightarrow\alpha\beta} = \begin{bmatrix} 1 & 0 \\ \frac{1}{\sqrt{3}} & \frac{2}{\sqrt{3}} \end{bmatrix}, \tag{12}$$

$$T = \begin{bmatrix} \cos(\theta) & \sin(\theta) \\ -\sin(\theta) & \cos(\theta) \end{bmatrix}, T^{-1} = \begin{bmatrix} \cos(\theta) & -\sin(\theta) \\ \sin(\theta) & cos(\theta) \end{bmatrix} \tag{13}$$

There are two methods by which rotor field orientation can be achieved i.e. Indirect Field Oriented (IFO) control and Direct Field Oriented (DFO) control as shown in Fig. 1 and Fig. 2 respectively. These two methods differ in the technique to calculate the angle θ_e necessary for field orientation. In a field oriented drive system, the *direct current* (i_{ds}^*) which is aligned along *d-axis* and *quadrature current* (i_{qs}^*) which is aligned along *q-axis* control flux and torque respectively. These two phase current input serve as the reference signal for the PI controller as shown in Fig. 1. The output from the PI controller is the corresponding voltage command in the *dq-reference* frame. The v_{ds}^* and v_{qs}^* are converted into three phase stationary reference frame using θ_e.

2.1.1. Indirect field oriented control. Indirect field oriented control was first proposed by Hasse [8] according to which Eq. 14 is necessary and sufficient condition for field orientation i.e. the entire rotor flux λ_r is aligned along d-axis and λ_{qr} is zero.

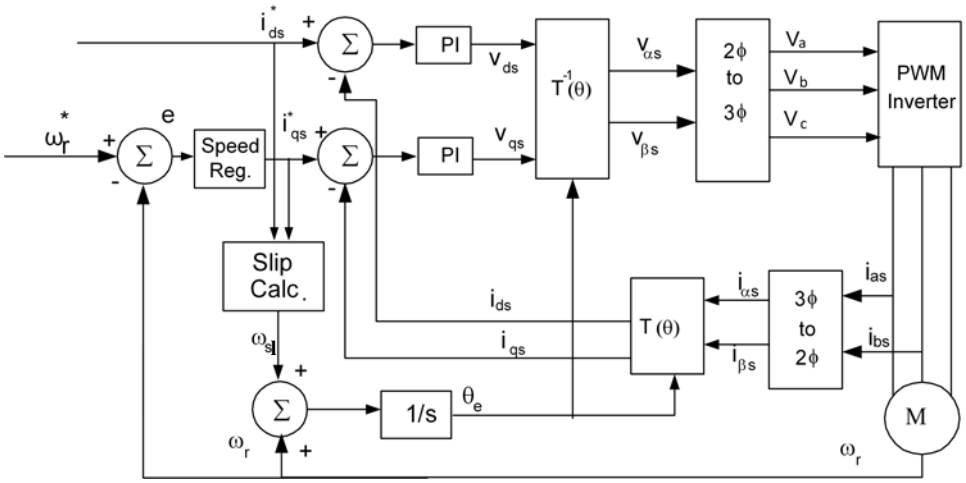

Figure 1: Control structure of IFO drive system

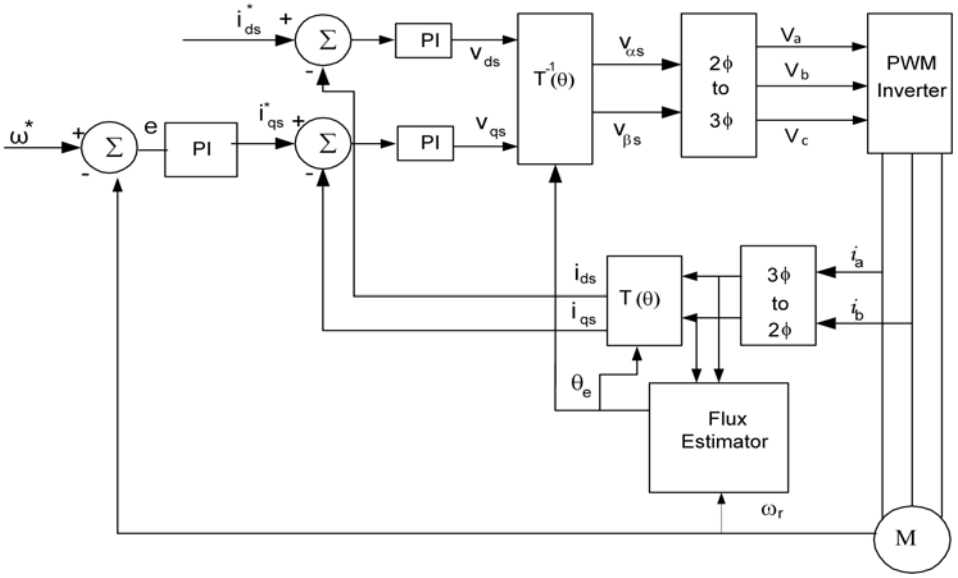

Figure 2: Control structure of DFO drive system

Then ω_e can be calculated from i^*_{ds} and i^*_{qs}, as shown in Fig. 3, which is integrated to get θ_e. This method is called indirect because it does not require explicit information about the rotor flux.

$$\omega_{sl} = \frac{i^*_{ds}}{i^*_{qs} T_r} \tag{14}$$

The electromagnetic torque (T_e) for an IFO drive system and induction motor mechanical model are represented by Eq. 15 and 16 respectively.

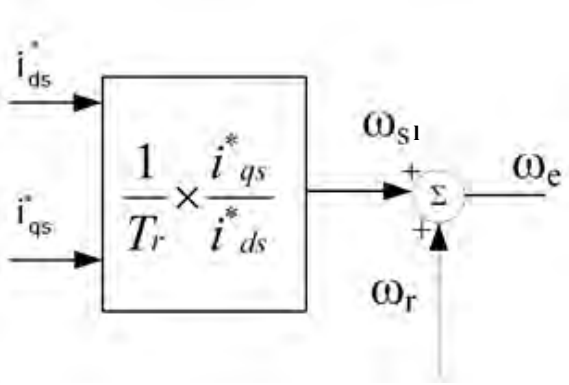

Figure 3: Slip calculation in IFO drive system

$$T_e = \frac{pL_m^2}{2L_r} i_{ds}^* i_{qs}^* \tag{15}$$

$$J\frac{d\omega_r}{dt} = T_e - B\omega_r \tag{16}$$

In these equations, 'L_m' is the mutual inductance, 'L_r' is the rotor inductance, 'i_{ds}^*' is the flux current command, 'p' is the number of pole pairs, 'J' is the motor inertia, and 'B' is Coulomb friction. Equations 15 and 16 are used to derive the open loop transfer function which relates the motor output speed (ω_r) and torque command current (i_{qs}^*). This transfer function is given by Eq. 17. An approximation of this transfer function is obtained by the first order plus dead time model (FPDT) given by Eq. 18 where 'L' is the dead time, 'T' is the time constant and 'K_{proc}' is the process gain. The parameters 'L', 'T' and 'K_{proc}' are determined from the step speed response. A step command current i_{qs} is applied to the induction motor working in open loop that produces a step speed response. This step response is used to approximate the FPDT model [52] given in Eq. 18. This system will be used later in chapter 4 for designing the fractional order PI controllers.

$$G_p(s) = \frac{\omega_r}{i_{qs}} = \frac{\frac{p}{2}\frac{L_m^2}{L_r} i_{ds}^*}{Js + B} \tag{17}$$

$$G_{approx}(s) = \frac{K_{proc}}{Ts+1} e^{-Ls} \tag{18}$$

2.2. Simulation Results

The indirect field oriented induction motor drive system is simulated in SIMULINK environment as is shown in Fig. 4. The *'Current Regulator'* is composed of two PI controllers for the regulation of i_{ds}^* and i_{qs}^* (Fig. 4). The three phase inverter consists of six switches and the gating signals are generated based on either SPWM or square wave technique. The AC machine is a three phase induction motor with the machine parameters given in Table 1. More information about the individual blocks in Fig. 4 is given in Appendix B. For this simulation, SPWM is used to generate the required PWM signals. The flux is established from the flux producing current command, i_{ds}^* and speed regulation is achieved from a PI controller which generates the i_{qs}^* for current regulator. The design of PI controllers for both current regulation and speed regulation is achieved by trial and error tuning. The design of speed controller will be explored further in chapter 4. The current regulator for i_{ds}^* is first tuned to obtain an acceptable step response followed by the tuning of the i_{qs}^* and speed regulators.

Table 1: Induction motor parameters

V_{LL}	415 V	Maximum current	0.4 A
Power	175 W	Rated speed	1475 RPM
L_{ls}	145.5 mH	L_{lr}	122.5 mH
L_m	750.9 mH	poles	4 (2 pole pairs)
R_s	47.5Ω	R_r	32 Ω

In order to test the performance of the drive system the step response, plotted in Fig. 5, of the system is analyzed. The flux is first established with a step current command i_{ds}^* of 0.4 A. The step response for i_{ds}^* is plotted in Fig. 6. Once the flux has been established, a speed command (ω_r^*) of 1000 RPM is used to validate the speed loop performance as shown in Fig. 5. It can be seen from the plot that the controller is able to completely follow the reference. The overshoot is also marked on the Fig. 5. The speed overshoot of 108 RPM translates to about 10%. The i_{ds} is plotted in Fig. 6

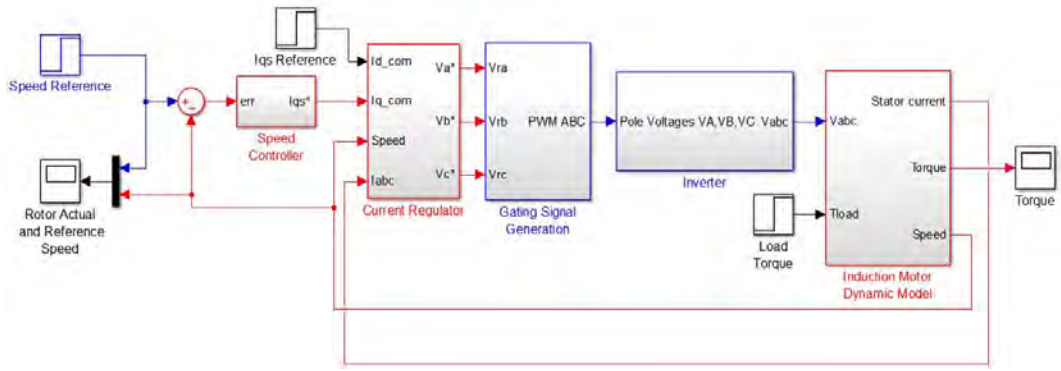

Figure 4: Simulation model for IFO drive system

for a step reference of 0.4 A and Fig. 7 shows the i_{ds} in the steady state condition. In the steady state the current is regulated within a band of about 0.04 A.

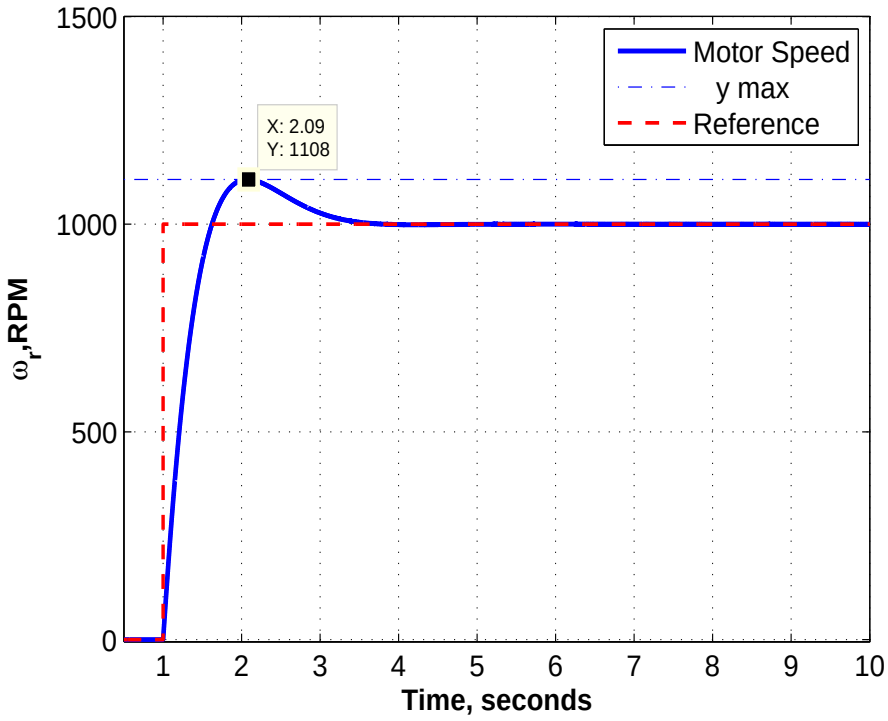

Figure 5: IFO step response in simulation

The torque command current (i_{qs}) and its tracking are plotted in Fig. 8 for the step speed command and Fig. 9 shows the reference and actual i_{qs} in steady state. The current controller is able to regulate the current within a band of 0.07A. The balanced three phase line currents in the stationary frame of reference are plotted in Fig. 10.

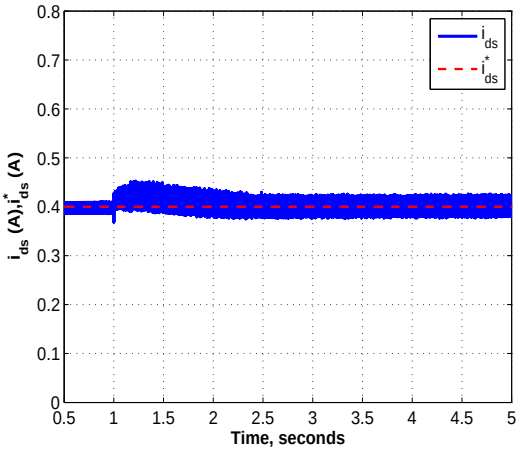

Figure 6: Direct axis (i_{ds}) current

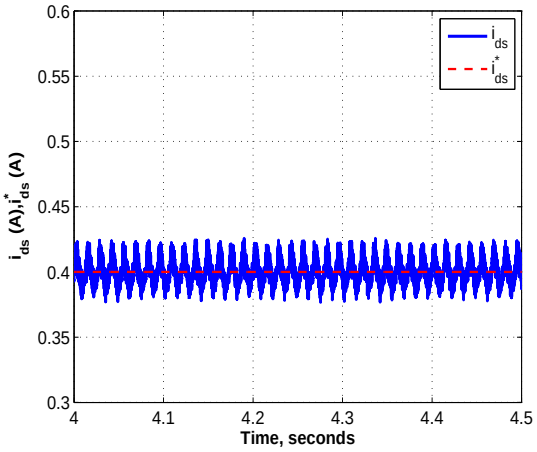

Figure 7: Direct axis (i_{ds}) current (Zoomed)

Only phase a and b line currents are shown in Fig. 10. The line currents i_a and i_b differ in phase by 120^o, as shown in the zoomed Fig. 11. The rotor flux in $\alpha - \beta$ reference frame is plotted in Fig. 12 and zoomed version in the steady state is plotted in Fig. 13.

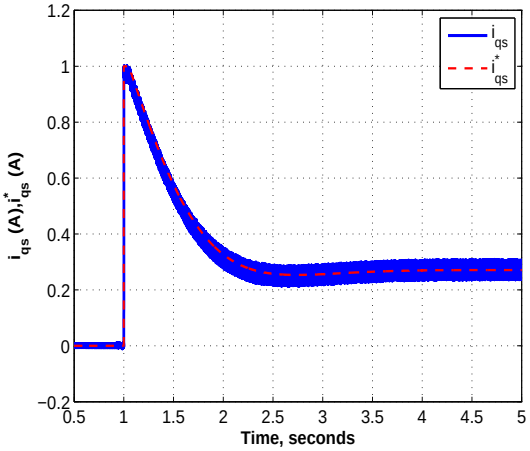

Figure 8: Quadrature axis (i_{qs}) current

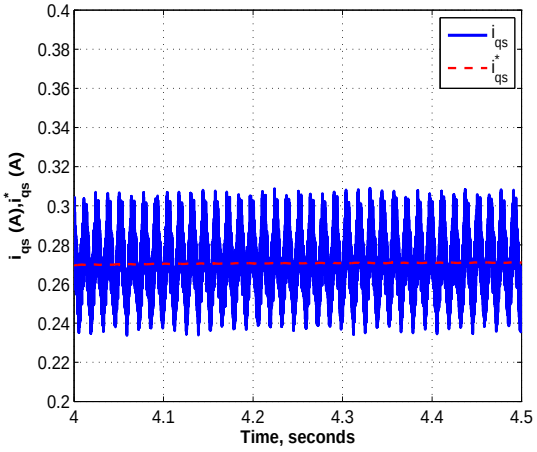

Figure 9: Quadrature axis (iq_{ds}) current (Zoomed)

2.3. Practical Implementation

Indirect field oriented control is implemented using dSPACE 1103 on the 175 W LabVolt induction motor. The parameters of the induction motor are determined using the no-load test, DC test and locked rotor test and the parameters are shown

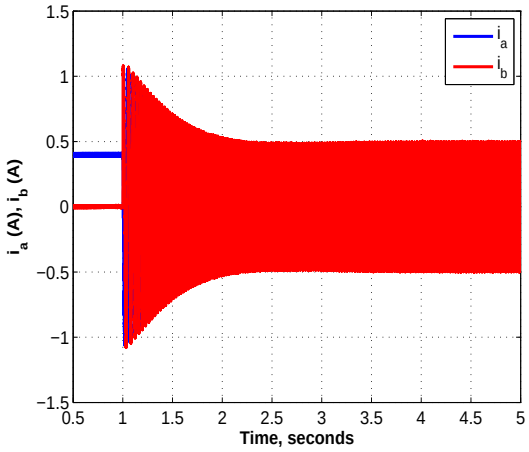

Figure 10: Line currents (i_a, i_b)

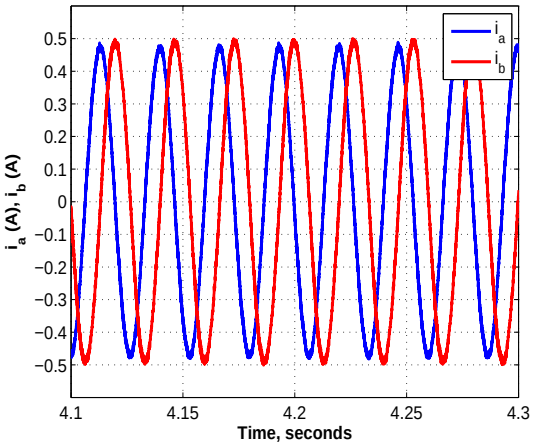

Figure 11: Line currents (i_a, i_b) (Zoomed)

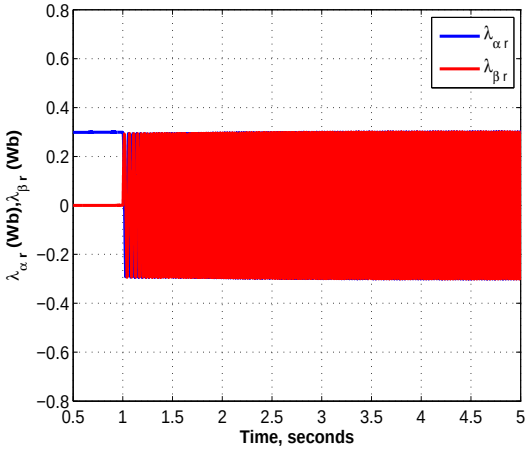

Figure 12: Rotor flux ($\lambda_{\alpha r}, \lambda_{\beta r}$)

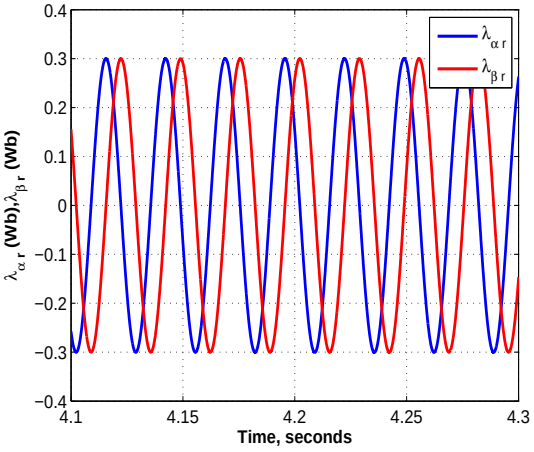

Figure 13: Rotor flux ($\lambda_{\alpha r}, \lambda_{\beta r}$) (Zoomed)

in the Table 1. The stator resistance is calculated using the DC test and the stator inductance, rotor resistance and inductance and mutual inductance of the motor are calculated using the no-load and locked rotor tests. The slip calculation, which is at the heart of IFO drive, is performed using the feed-forward operation described by Fig. 3 which essentially implements Eq. 14. The overall IFO drive system is depicted in Fig. 1. The flux is regulated by establishing a current command i^*_{ds} using a proportional integral (PI) controller. The speed is regulated by using a cascaded control structure where the first PI controller generates a quadrature current (i^*_{qs}) command. The i^*_{qs} is than regulated by a separate PI controller. The controllers for i^*_{ds} and i^*_{qs} generate the voltage commands v^*_{ds} and v^*_{qs} respectively. The electrical frequency (ω_e) calculated

using Eq. 14 is integrated to obtain the electrical angular position (θ_e) of rotor flux vector which is used to perform coordinate transformation from stationary reference frame to synchronously rotating (dq) reference frame and vice versa. These voltages (v_{ds}, v_{qs}) converted to the stationary frame (v_a^*, v_b^*, v_c^*) serve as the reference waveforms to generate PWM signals for inverter operation.

2.3.1. Test setup. The hardware setup shown in Fig. 14 is constructed for real time implementation. This system uses LabVolt modules and the details of each module is tabulated in Table. 2. More information related to these modules can be seen in Appendix A. The current sensors used in the experiments is manufactured by LEM with the part number 'LA-25NP'. These sensors have the maximum current measuring capability of 25 A. The selected drive system has a nominal current rating of 0.6 A and therefore, the current is not expected to exceed this limit. For tuning these sensors, the voltage measured by the analog to digital converter (ADC) i.e. V_{adc} of dSPACE 1103 and the actual current are compared and linear curve fitting is used to obtain the best approximation of the measured current $I_{measured}$. The plot in Fig. 15 shows this procedure for one of the current sensors and the associated current measurement equation in dSPACE.

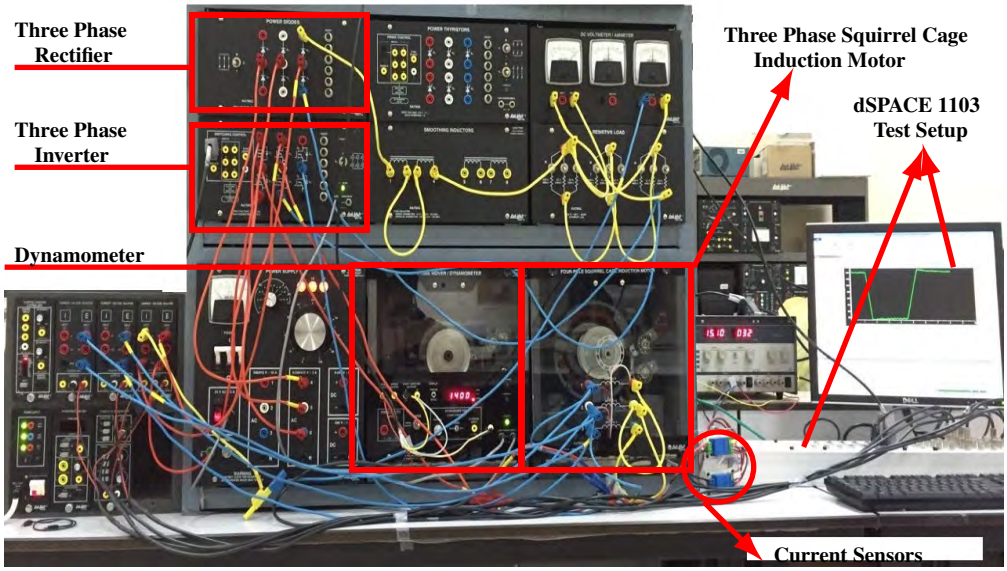

Figure 14: Experimental setup for the IFO drive system

Table 2: Test set-up modules

No.	Module	Module No.	Description
1	Induction Motor	LabVolt 8221-0A	175 W three phase squirrel cage induction motor
2	Three phase inverter	LabVolt 8837-0A	Inverter for controlling the motor speed
3	Dynamometer	LabVolt 8960-15	To add mechanical load to the motor and measure the motor speed
4	Diode rectifier	LabVolt 8842	Used as an uncontrolled diode rectifier to convert the fixed 415 V AC power to DC
5	Inductor	LabVolt 8325-15	Used as a smoothing filter for the DC bus to remove the ripples from the output of the uncontrolled rectifier
6	Resistive bank	LabVolt 8311-0A	Used at the DC bus
7	Current sensor	LEM LA-25 NP	Used in the feedback loop for the IFO implementation
8	Power supply	LabVolt 8821-2A	Used as a variable power supply for the drive system

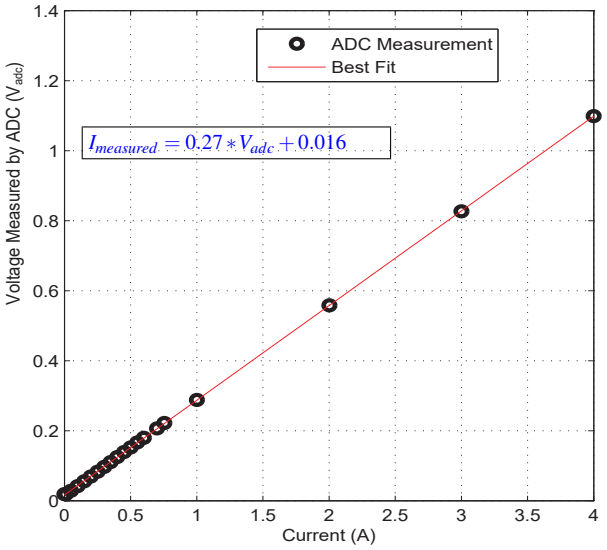

Figure 15: Current sensor tuning

A block diagram constructed in SIMULINK, as shown in Fig. 16, is interfaced with Control Desk. The speed controller is a proportional integral (PI) controller in this experiment and is implemented in the block 'FO-PI or IO-PI Speed Controller'. The

PI controllers for the regulation of i_{ds} and i_{qs} are implemented in 'Ids PI controller' and 'Iqs PI controller' respectively as shown in Fig. 16. The command voltages v^*_{ds} and v^*_{qs} generated by PI regulators are transformed into three phase stationary reference frame. The block 'Gating Signal Generation' generates the PWM pulses necessary for the operation of three phase inverter using any mode of operation i.e. SPWM or square wave. The slip calculation (Eq. 14) is implemented as depicted in Fig. 3. The encoder available for this setup has 360 pulses.

The step speed response when tested with the Lab Volt system is shown in Fig. 17. The sampling frequency is set at approximately 18 kHz while the switching frequency of the inverter is set constant at 1 kHz. A direct current command (i^*_{ds}) command of 0.3 A is first applied to the motor to set up initial flux. After the flux has been established and the current is stabilized, a speed reference of 500 RPM (ω^*_r) is applied to test the step response of the system and the corresponding results are plotted in Fig. 17.

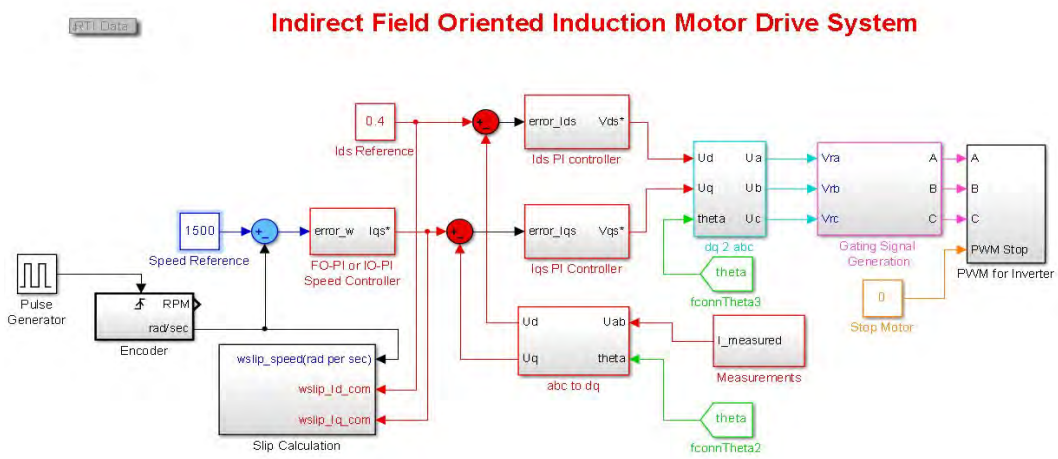

Figure 16: IFO dSPACE-SIMULINK model

The motor line currents when the speed is set at 500 RPM are plotted in Fig. 18. The two line currents, i_a and i_b, differ in phase by 120^o. The third line current i_c can be determined from the Eq. 19. The performance of cascaded PI controllers can be evaluated by observing the tracking performance of the controllers. The actual

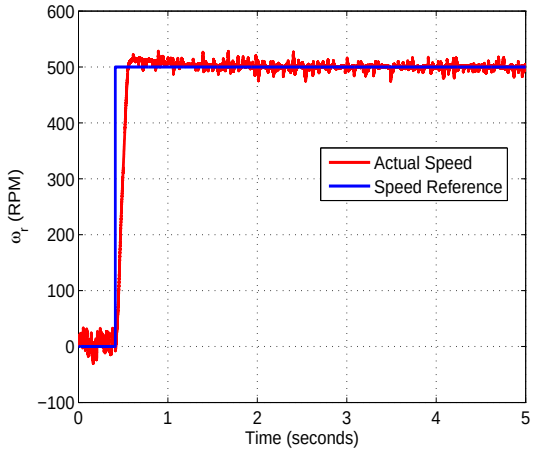

Figure 17: Speed (ω_r) RPM

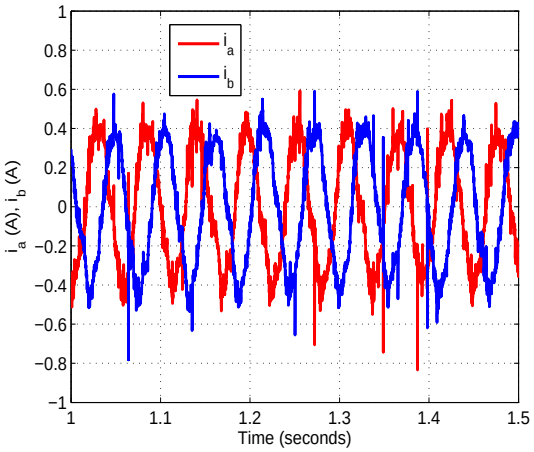

Figure 18: Line currents (i_a, i_b), A

and command flux producing current i_{ds} are plotted in Fig. 19 while the torque current command i^*_{qs} and actual current i_{qs} are plotted in Fig. 20.

$$i_a + i_b + i_c = 0 \tag{19}$$

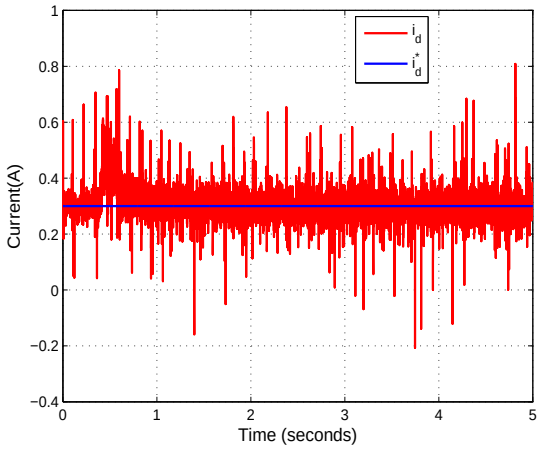

Figure 19: Direct axis (i_{ds}) current

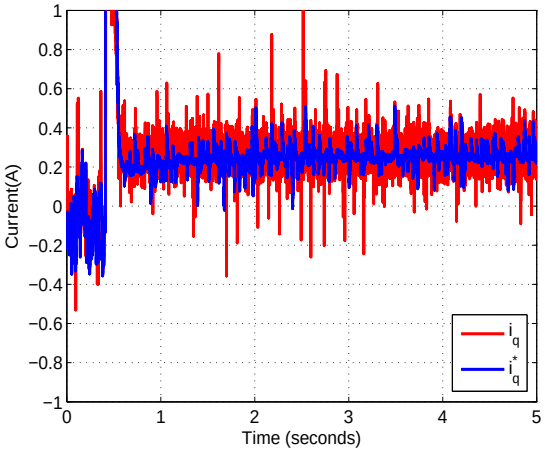

Figure 20: Quadrature axis (i_{qs}) current

Chapter 3: Three Phase Inverter Control

The three phase inverter is usually operated in sine triangle pulse width modulation (SPWM) or space vector pulse width modulation (SV-PWM) mode of operation. However, for high speed, high power operation square wave or 180^o conduction mode is preferred. In this work, only SPWM and square wave modes are considered and implemented. It has been mentioned in the literature that benefiting from both of these switching modes i.e. SPWM and square wave mode of operation, enhances the drive system performance throughout the entire speed range of the motor. Therefore, a new method of mode switching between the SPWM and square wave is presented which ensures lower torque ripples during inverter mode switching.

Synchronous sine triangle pulse width modulation is an extension of SPWM where the carrier frequency is kept an integer multiple of fundamental frequency of the motor. Synchronizing the carrier frequency with the fundamental frequency reduces the sub-harmonics, hence the total harmonic distortion (THD). Moreover, the motor losses also decrease with the increase in carrier frequency. The switching losses in the inverter, on the other hand, increase in direct proportion to the carrier frequency. Therefore, the carrier frequency, also called as the switching frequency, should be adjusted to reduce both the switching losses and harmonic losses. The three phase inverter consists of six switches that are arranged in the configuration shown in Fig. 21. The two switches in each leg cannot be switched ON at the same time otherwise it will short circuit the DC bus resulting in a very high current known as the shoot-through current. Therefore, the switching signals of two switches in each leg should always be complemented.

3.1. Sine Triangle Pulse Width Modulation (SPWM)

The SPWM mode of operation produces a much better approximation of a sinusoidal waveform. The concept of SPWM arises from the fact that the output waveform is produced by switching the switches based on the comparison of a sinusoidal reference signal with a triangular signal commonly known as the carrier signal. The output voltage consists of pulses while the output current better matches with a sinusoidal signal as compared to the square wave voltage signal. The frequency of the carrier signal

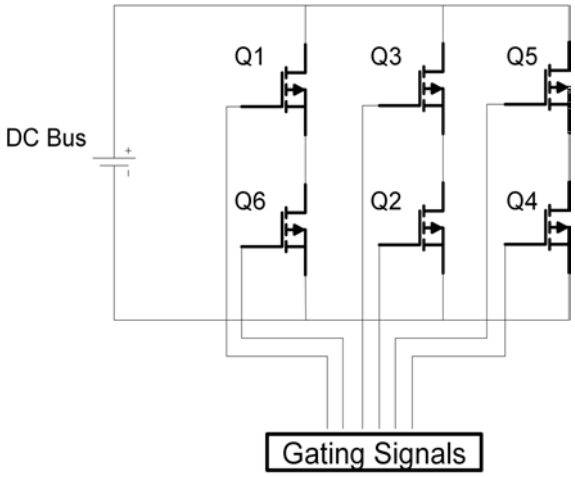

Figure 21: Three phase inverter

is kept higher as compared to the reference signal. The most profound benefit of such a scheme is that it shifts the harmonics to multiples of carrier frequency which are usually of the order of several kHz, as shown in Eq. 20. The harmonics, therefore, are shifted to the multiples of this frequency and hence can be easily filtered from inverter output. The filters required for the removal of these harmonics are smaller and less expensive than those required for the square wave inverter.

$$\begin{aligned} f_h &= (jf_c \pm k)\, f_1 \\ j = 1,3,5\cdots for\, k &= 2,4,6\cdots \\ j = 2,4,6\cdots for\, k &= 1,5,7\cdots \end{aligned} \tag{20}$$

The inverter with sine triangle pulse width modulation (SPWM) mode of operation is implemented in both simulation and experimentation. SPWM is implemented by comparing a triangular carrier signal with a sinusoidal reference signal. For the three phase inverter, three such signals each displaced by 120^o are compared with the same triangular carrier signal. Changing the frequency and the magnitude of the reference signals changes the speed of the induction motor. The proportional integral (PI) controller regulates the speed of the motor by varying the magnitude and frequency of the reference signal. SPWM performs better at low speed but Eq. 21 shows that the DC bus utilization is low as compared to square wave mode of operation which can be seen in Eq. 22.

$$V_{fundamental,RMS} = 0.612 m_a V_{dc} \tag{21}$$

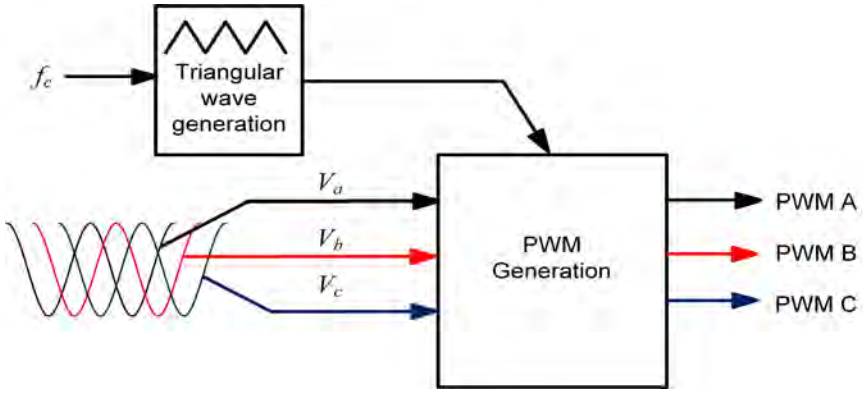

Figure 22: SPWM gating signal generation

3.2. Square Wave Inverter

The square wave inverter, also called the six step inverter, generates a six step square wave line to line voltage whose fundamental component is sinusoidal. The conversion from DC to AC signal is achieved by keeping each switch ON for exactly half of the period. The order in which the MOSFETs are switched, results in the square wave output phase voltage. The gating signals are generated according to the pattern plotted in Fig. 23. The signals 'G_1', 'G_2' and 'G_3' are for the first switch of each leg of the inverter while the gating signal for the second switch in each leg is the complement of these signals [53]. When used for speed control of induction motors, the time period of these signals decide the motor speed.

The Fourier analysis of the line to line voltage shows that it consists of all odd harmonics except the triplen harmonics. Therefore, the most dominant harmonics are the fifth and seventh harmonics. The presence of harmonics close to the fundamental frequency of the motor increases the total harmonic distortion as well as the harmonic losses in the machine. This effect is prominent at low speeds because the motor leakage reactance is comparatively lesser than the reactance at high speed which results

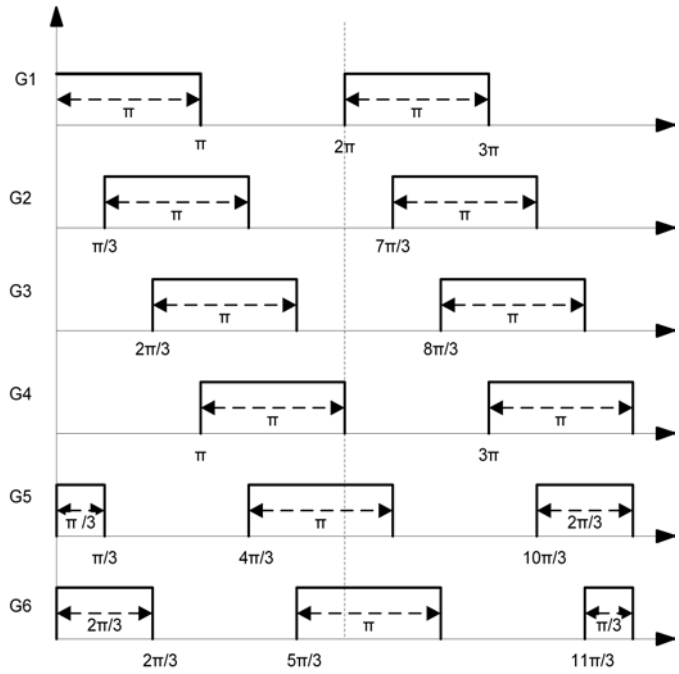

Figure 23: Gating signals for square wave mode of operation

in higher harmonic current. Moreover, the harmonics appear close to the fundamental frequency thereby are difficult to remove.

The square wave inverter is beneficial for high speed operation of induction motor drive system because of its higher DC bus utilization. The root mean squared (RMS) fundamental component for a square wave drive is given by Eq. 22. The maximum fundamental output line to line voltage that can be obtained from this type of inverter is 0.78 times the available DC bus which is higher than that obtained for SPWM or even SV-PWM inverters.

$$V_{fundamental,RMS} = \frac{\sqrt{6}}{\pi} V_{dc} = 0.78 V_{dc} \tag{22}$$

3.3. Synchronous Sine Triangle Pulse Width Modulation

The SPWM relies heavily on the switching frequency of the inverter which is the same as the carrier frequency used to generate the PWM signal for the switches. Harmonic losses in the machine depend upon the carrier frequency of the motor. Increasing the carrier frequency shifts the harmonics that appear at multiples of carrier

frequency to the high frequency range. For variable speed drives that can operate in high frequency range, carrier frequency of the inverter must be increased with increasing speed of the motor in order to keep the same order of the harmonics. Moreover, this avoids high switching losses in the inverter at low speed and reduces harmonics and motor losses during high speed operation of the induction motor drive system.

The motor losses can be reduced by synchronizing the carrier frequency with the fundamental frequency of the motor. Moreover, synchronizing the carrier frequency of the inverter with the fundamental frequency removes sub-harmonics in the machine and therefore further improves the drive system performance. The synchronization is achieved by converting the ω_e obtained from slip calculation, into the fundamental frequency as shown in Fig. 24. The product of calculated f_e and a suitable number 'm' results in the frequency of the carrier signal (f_c). The triangular signal is generated with the frequency f_c and compared with the sinusoidal reference signals to obtain the required PWM signals.

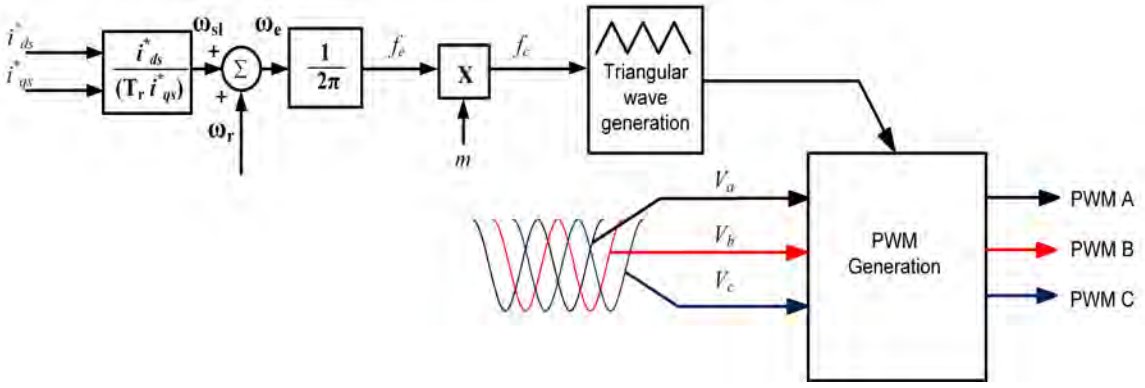

Figure 24: Synchronous SPWM generation

3.4. Hybrid Mode Switching

In order to benefit from both switching modes, a switching scheme is devised that uses SPWM below the base speed and square wave mode of operation above the base speed. Both PWM schemes depend upon the generation of their specific PWM signals. Simply switching from one scheme to the other can potentially disrupt the current

and can cause torque ripples in the machine. This momentary disruption is undesired for motion control applications and therefore such a transition must be avoided. The conventional mode switching is depicted in Fig. 25. When the mode is switched, the sinusoidal reference is ignored, as shown in Fig. 25 (a), and the gating signals for six-step mode are used to operate the three phase inverter (Fig. 25 (b)). The discontinuity in the PWM signal results in torque ripples and degrades the drive performance.

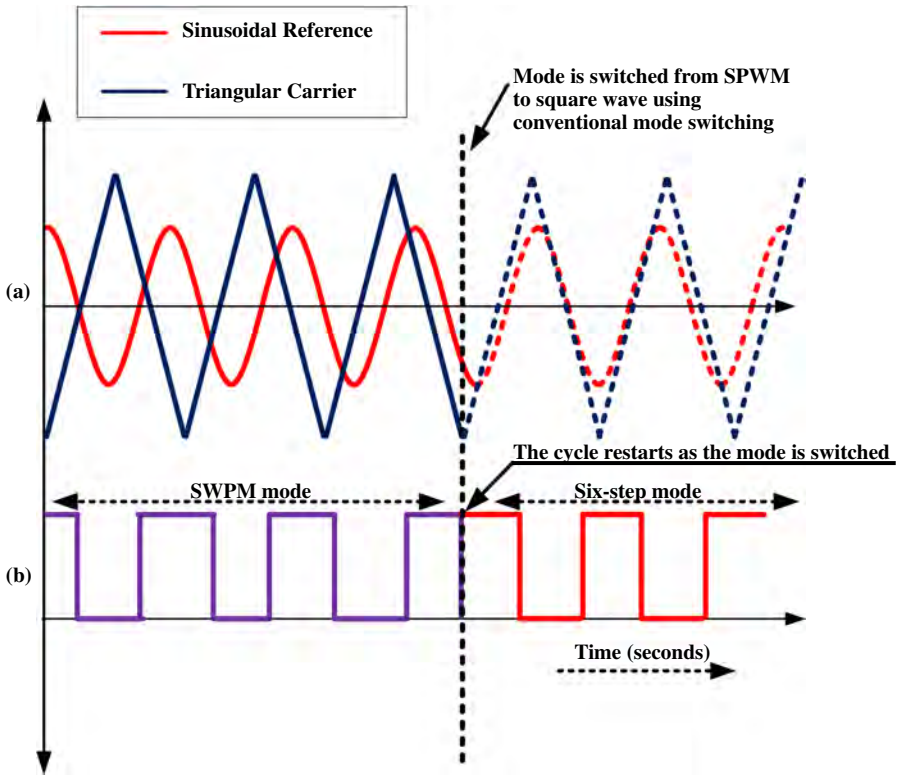

Figure 25: Mode switching

A hybrid mode switching technique is proposed which is achieved by simply forcing the carrier frequency to zero. The generation of SPWM depends upon the comparison of the triangular carrier signal with the sinusoidal signal. Square wave mode of operation can also be implemented in the same way as SPWM by comparing the sinusoidal signal with a zero magnitude triangular signal. When this zero triangular signal is compared with the sinusoidal reference signal, the resultant switching waveform is the same as required for square wave mode of operation. Therefore, a seamless transition can be realized by forcing the carrier to zero. This technique does not disturb

the voltage and current cycle during the mode switching which results into seamless transition between the two modes of operation and reduces the motor torque ripples. The hybrid mode switching is depicted in Fig. 26. The carrier frequency, in Fig. 26 (a), is forced to zero as the mode is switched thereby eliminating the discontinuity in the PWM generation as shown in Fig. 26 (b). Moreover, it reduces the computational overhead required for the implementation of a separate six-step PWM generation.

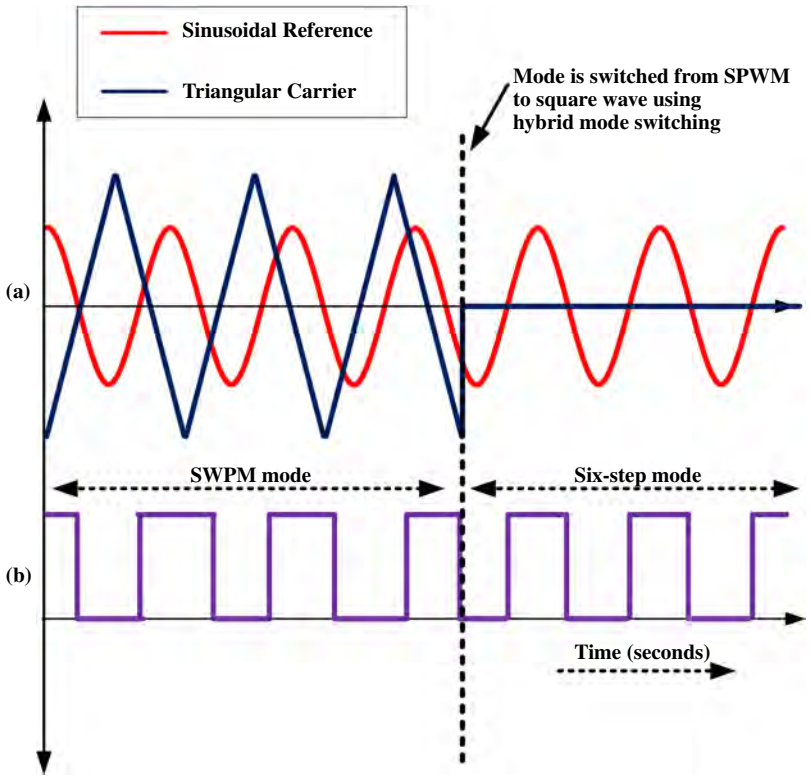

Figure 26: Hybrid mode switching

3.5. Implementation of SPWM

The SIMULINK block is developed for the practical implementation of SPWM mode of operation. The structure shown in Fig. 27 generates the gating signals necessary for SPWM mode of operation. The block 'Fundamental Based Carrier Generation' generates the carrier signal of a desired frequency programmed as an input in the controller. The output is fed to the 'Hybrid Mode Switching' block for the implementation of a seamless transition from SPWM to square wave mode. 'PWM Generation' com-

pares the output of the 'Hybrid Mode Switching' with the three reference signals 'V_{ra}', 'V_{rb}' and 'V_{rc}' to generate the gating signals for the three legs of the inverter. In order to make this scheme synchronized, the carrier signals is made an odd integer multiple of the fundamental frequency of the motor. The step speed response, line currents and performance of the controller have already been discussed in chapter 2. The following section discusses the practical implementation of SPWM.

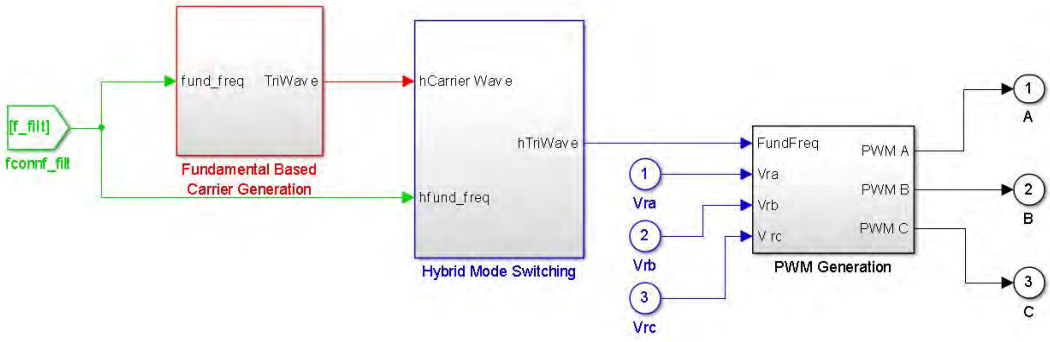

Figure 27: SPWM gating signal generation for IFO drive system

The simulation and real time implementation of the synchronous SPWM is realized by maintaining a linear relationship between the carrier frequency and the fundamental frequency. The fundamental frequency is determined from the slip compensation used for indirect field orientation and measured motor speed. The 'ω_e' determined from IFO (Eq. 14) is multiplied with ($\frac{1}{2\pi}$) to get the fundamental frequency 'f_e' of the motor as shown in Fig. 28.

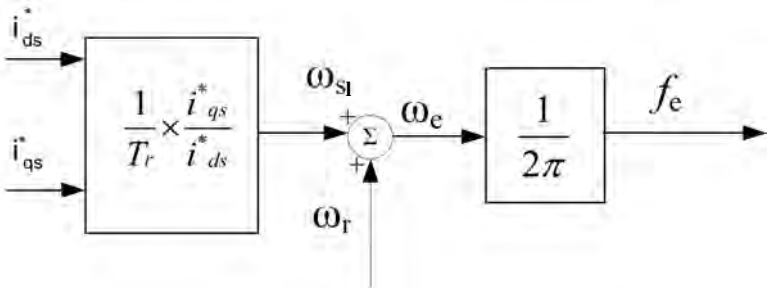

Figure 28: f_e calculation

3.6. Proposed Optimum Carrier Frequency Control

Synchronization automatically ensures linearly increasing frequency with the increase in fundamental frequency of the inverter. But the motor losses may not always linearly change with the change in carrier frequency because these losses depend upon the construction of the iron core [29] as well. In order to determine the frequency which produces minimum losses, the currents and voltages applied to the machine must be analyzed. It is found that the fundamental component of the line currents and voltages change with the carrier frequency at the same speed. At the same speed, different carrier frequencies result in different fundamental components of currents and voltages. An optimum carrier frequency at a specific speed is the the carrier frequency that results in lower fundamental components of voltages and currents.

This work will investigate the selection of optimal carrier frequency based on the fundamental component of line current and will construct a function that will provide optimum carrier frequency for a specific speed. A similar technique must be followed to determine the optimum carrier frequencies at different speeds. For reduction of harmonic losses the motor must be operated at these optimum carrier frequencies.

3.7. Simulation Results

Simulations are performed on the 175 W prototype induction motor setup developed previously in chapter 2. Mode switching is implemented by the comparison of the sinusoidal signals with zero carrier signal. The sinusoidal signals are generated with the frequency f_e determined from the slip calculation shown in Fig. 28. Comparison of the three sinusoidal signals with zero will generate the PWM for the three legs of the inverter. The mode switching is tested in simulation by setting the speed of the motor to 1400 RPM and consequently switching the mode in steady state. In Fig. 29, the motor is running at 1400 RPM and the mode is switched at 5 seconds. An overshoot of 246 RPM is observed as the inverter mode of operation is switched from SPWM to six-step mode. The speed returns to the set reference of 1400 RPM after approximately 1.5 seconds. Moreover, a transient in the torque is observed i.e. the torque momentarily approaches 1.8 Nm. The switching from SPWM to six-step is more visible in the cur-

rent and voltage plots shown in Fig. 30 (c) & (d). The current changes from sinusoidal to six-step when the mode is switched as shown in Fig. 30 (c) and the line voltage (V_{ab}) changes from PWM to square wave as shown in Fig. 30 (d).

The hybrid mode switching is tested in simulation for which the triangular carrier signal is generated with the predefined frequency for SPWM mode of operation. In order to switch from SPWM to square wave mode of operation, the carrier frequency is forced to be zero thereby causing the comparison of a zero signal with the sinusoidal references, each of them being 120° apart. This comparison automatically generates PWM pulses for square wave mode of operation.

The step response of the drive system for a step of 1400 RPM is shown in Fig. 31 and Fig. 32. The mode is switched for this simulation at $time = 5$ seconds. The carrier frequency goes to zero at this time and the inverter switches from SPWM to square wave mode of operation. The plot in Fig. 32 shows the transition from SPWM to square wave mode of operation in the step response of Fig. 31. The transition is smooth and seamless as compared to simple mode switching and produces lower torque ripples

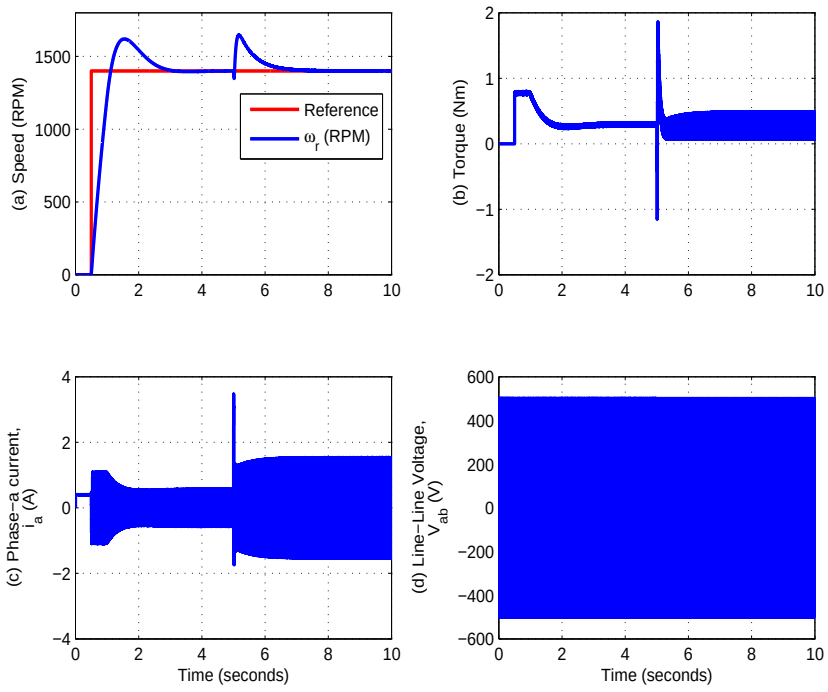

Figure 29: Simulation results for conventional mode switching at 1400 RPM (a) Speed, ω_r (RPM), (b) Torque, τ (Nm), (c) Line current, i_a (A), (d) Line Voltage, V_{ab} (V)

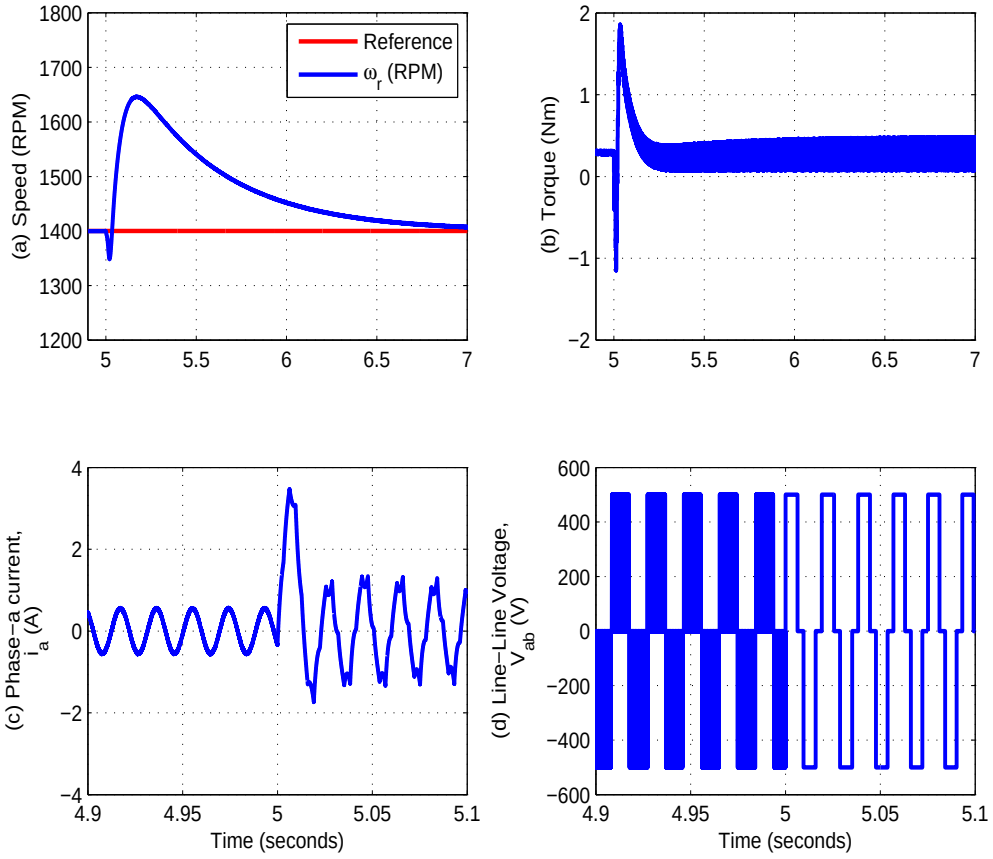

Figure 30: Simulation results for conventional mode switching at 1400 RPM (zoomed view) (a) Speed, ω_r (RPM), (b) Torque, τ (Nm), (c) Line current, i_a (A), (d) Line Voltage, V_{ab} (V)

in the machine. Furthermore, there is no cycle discontinuity i.e. the current cycle is not disturbed during switching.

3.8. Experimental Results

The synchronous PWM inverter with hybrid mode switching scheme is implemented for a field oriented induction motor drive system developed in Fig. 14.

3.8.1. Optimum carrier frequency operation. In order to determine optimum carrier frequencies at a particular speed, the frequency spectrum of line currents is analyzed. The fundamental component in the Fourier spectrum is recorded at different speeds. For a particular speed it has been found that the fundamental component

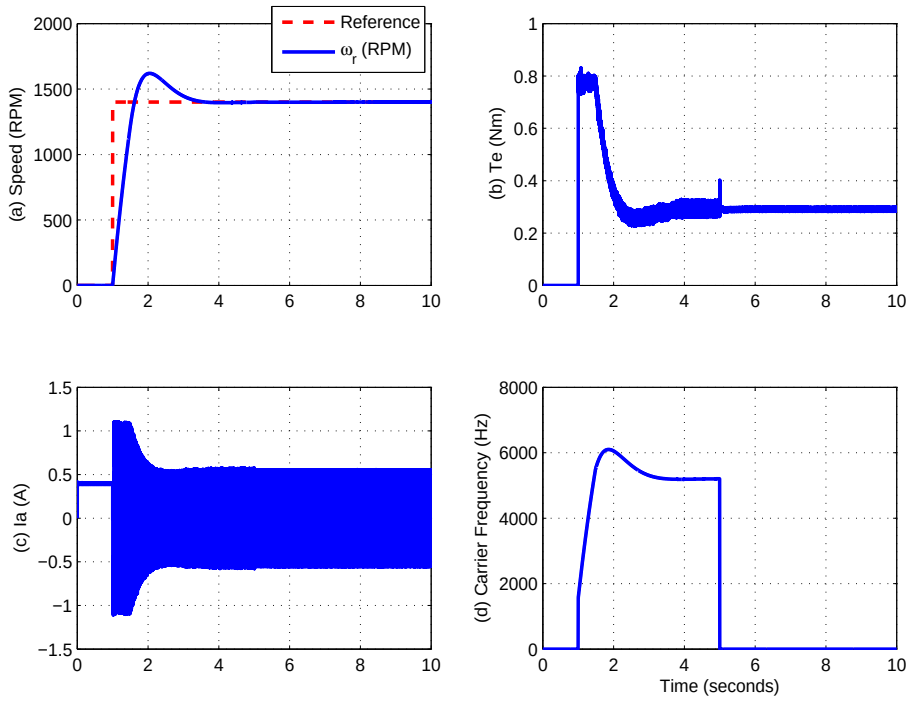

Figure 31: Simulation results for hybrid mode switching at 1400 RPM (a) Speed, ω_r (RPM), (b) Torque, τ (Nm), (c) Line current, i_a (A), (d) Carrier frequency, f_c (Hz)

is different at different carrier frequencies while the output mechanical power of the motor is the same. The reason being that, for the same amount of output power, if the motor draws higher input power then machine losses have increased.

The higher values of fundamental components is an indication of higher power drawn from the motor. An increase in the fundamental component can therefore be attributed to the increase in input power which further indicates higher harmonic losses in the machine. Therefore, operation of the induction motor at the frequency which will lead to lower motor losses ensures optimal machine performance. Table 3 compares the fundamental components of voltages and currents at 100 RPM and at different carrier frequencies. Fundamental components of voltage and current are minimum at the carrier frequency of 3064.1 Hz with the values of 40.1491 V and 0.2654 A respectively. Therefore, when the drive is operated at 100 RPM, the carrier frequency should be set at 3 kHz to minimize the harmonic losses in the machine.

A similar procedure is followed for 300, 500, 600, 700, 800, 900, 1000, 1200, 1500 (RPM) speed and the fundamental components are recorded. Fig. 33 shows the

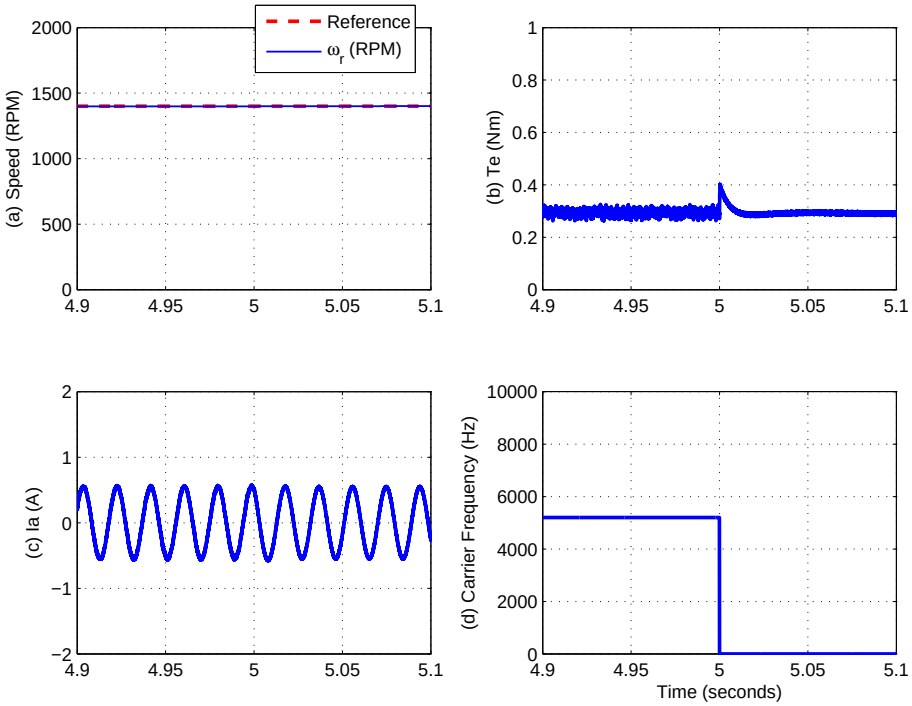

Figure 32: Simulation results for hybrid mode switching at 1400 RPM (zoomed view) (a) Speed, ω_r (RPM), (b) Torque, τ (Nm), (c) i_a (A), (d) Carrier frequency, f_c (Hz)

Table 3: Fundamental voltage and current components at 100 RPM

f_c	$f_1 v$	$f_1 i$
261.5	41.1410	0.2755
447.6	49.7535	0.3285
608.8	55.3384	0.3662
792.6	45.7888	0.3016
969.4	56.0391	0.3666
1320.9	55.8501	0.3674
1769.1	55.9973	0.3633
2210.9	42.1040	0.2799
2614.1	57.4428	0.3766
3064.1	40.1491	0.2654
3526.1	46.5334	0.3089
39630	46.3139	0.3007

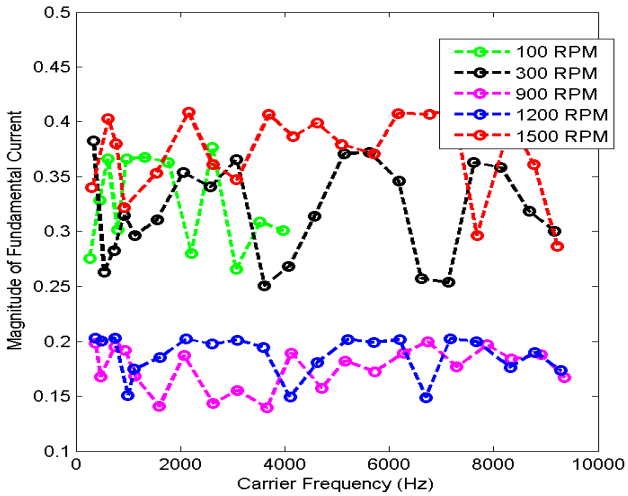

Figure 33: Changing fundamental with carrier frequency

Table 4: Optimum carrier frequencies at different speeds (experimental results)

Speed (RPM)	Carrier Freq (Hz)	Speed (RPM)	Carrier Freq (Hz)
100	3064	800	7354
300	3613	900	3652
500	2118	1000	8910
600	3167	1200	6705
700	4046	1500	9222

variation in the fundamental component at different speeds as the carrier frequency is varied from 300 Hz to 10 kHz which is the maximum allowable switching frequency of the inverter. According to Fig. 33, the magnitude of the fundamental component is the lowest for carrier frequencies of 8910 Hz, 6705 Hz and 9222 Hz for 900 RPM, 1200 RPM and 1500 RPM respectively. The machine should be operated at these frequencies to reduce the drive system losses. Similarly, the optimum carrier frequencies are determined for a wide speed range and Table. 4 tabulates the results.

It can be seen from the optimum carrier frequencies that as the speed increases, the optimum carrier frequencies may not always increase. The optimum carrier frequency at 500 RPM is 2118 Hz which is lower than the optimum carrier frequency at 100 RPM. If the carrier frequency is obtained by multiplying the fundamental frequency with '99', then the corresponding carrier frequencies are tabulated in Table. 5.

The frequencies selected by this linear function are different from the optimum carrier frequencies. Therefore, a linear function will be unable to provide these optimum frequencies.

Table 5: Comparison between optimum carrier frequency and the carrier frequency obtained from linear function

Speed (RPM)	Optimum carrier frequency (Hz)	Linear function (99) (Hz)
100	3064.1	433.818
500	2118	1751.31
1200	6705	4088.7
1500	9222	5080.68

The optimum carrier frequency is plotted in Fig. 34 to obtain an approximate synchronous function. Second order polynomial regression is used to get a best fit that matches the optimum carrier frequency data. The corresponding Eq. 23 ensures optimum carrier frequency operation while at the same time, maintains synchronism. This function is then modified to obtain Eq. 24, to make sure that the carrier frequency remains an odd integer multiple of 3 and maintains synchronism between the fundamental and the carrier frequency. The resulting function is tested for optimum carrier frequency operation.

$$f_c = 3\,(f_1) - 23.74\,(f_1) + 3250 \tag{23}$$

$$f_c = 3\,(f_1) - 24\,(f_1) + 3249 \tag{24}$$

The field oriented drive system with the proposed quadratic synchronous function is tested for the trapezoidal wave tracking. The results are shown in Fig. 35. The subplot Fig. 35(b) shows how the carrier frequency is adjusted by the function from 3 kHz to about 10 kHz while the speed changes from 300 RPM to 1400 RPM. The motor is able to completely track the reference with minimal steady state error as shown in Fig. 35 (a). The carrier frequency changes quadratically as shown in Fig. 35 (b).

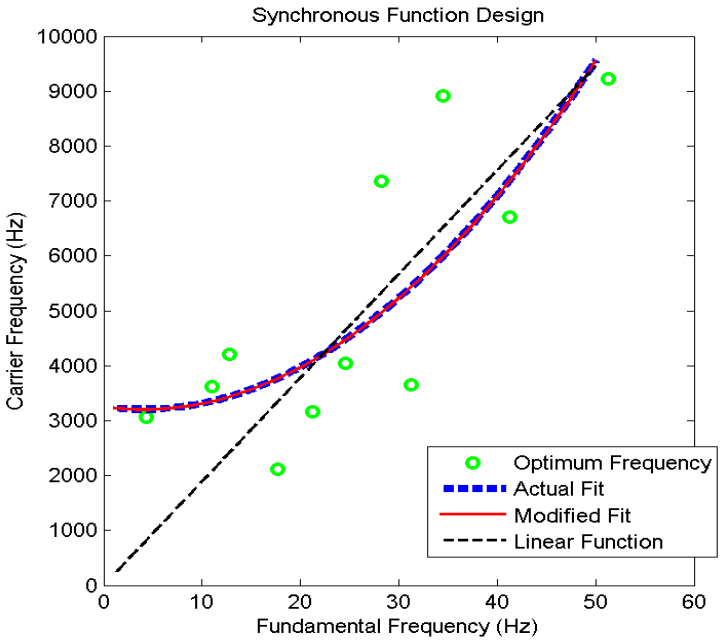

Figure 34: Determination of synchronous function using curve fitting

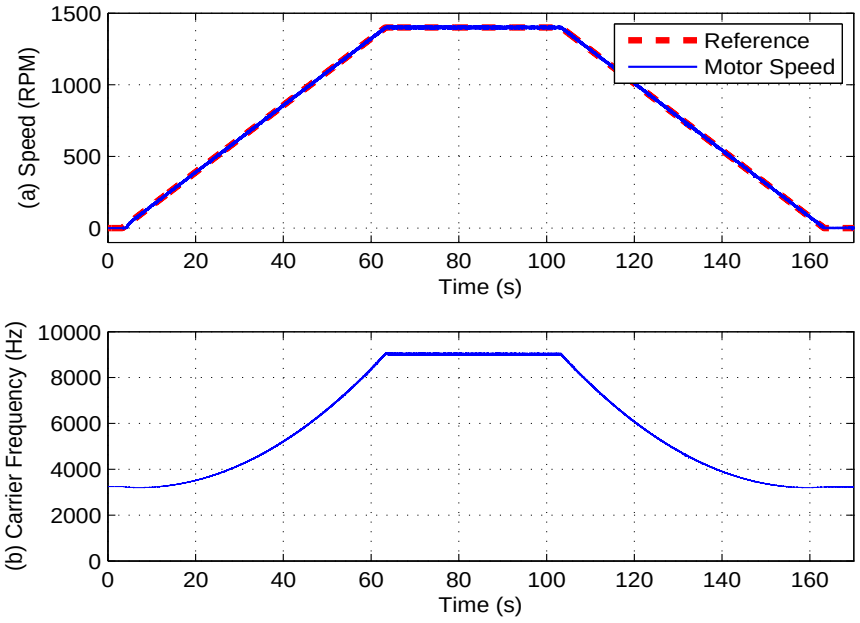

Figure 35: Optimum carrier frequency control

The line currents and line voltages when the system is operating under SPWM mode of operation are shown in Fig. 36. These plots have been zoomed over 0.3 seconds to be able to view the sinusoidal nature of line current and PWM pulses in the line voltage. It should be noted that the filtered line current and voltage are plotted in

Fig. 37 (a) and (b) respectively. The line voltage, in Fig. 37 (b), is the fundamental component of the line voltage and is a sinusoidal signal instead of the pulse width modulated signal plotted in Fig. 36 (b).

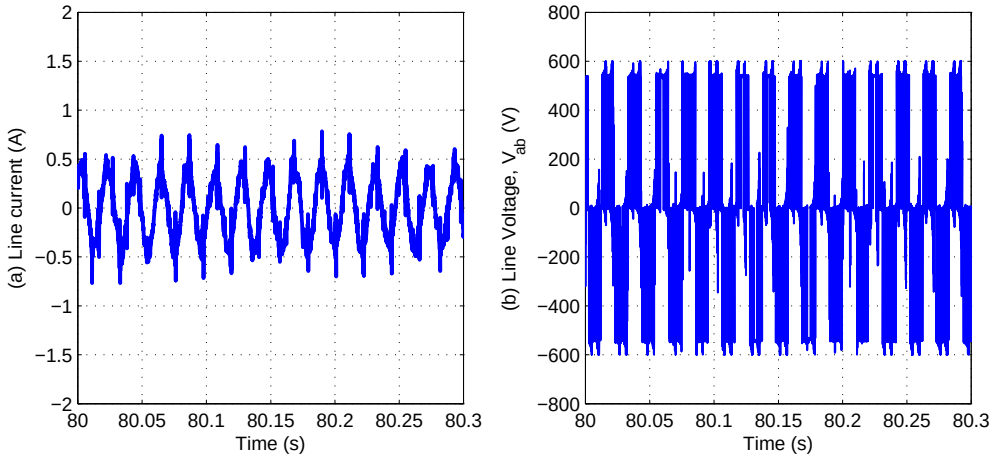

Figure 36: (a) Line current (i_a), A (b) Line voltage (V_{ab}), V

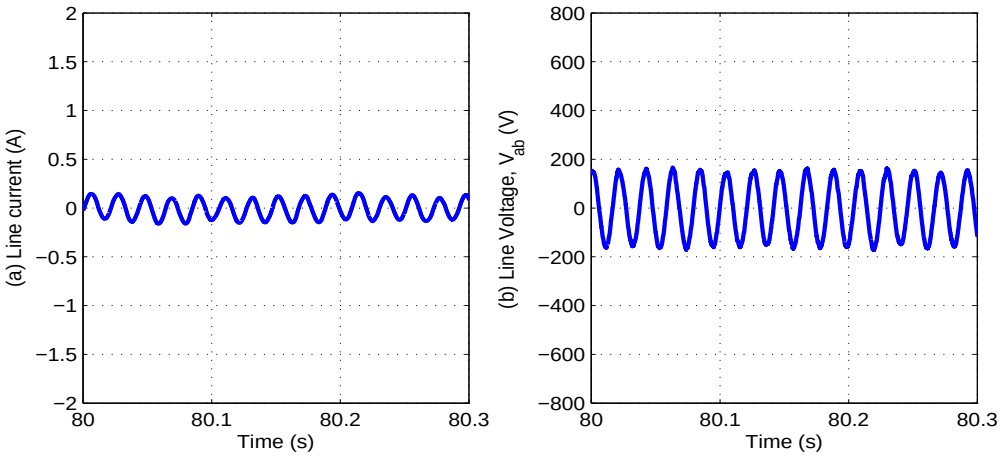

Figure 37: (a) Filtered line current (i_a), A (b) Filtered line voltage (V_{ab}), V

The operation of field oriented drive system working under the synchronous function is evaluated and compared with the operation of the three phase inverter fed induction machine working with linear function. The linear synchronous function is designed based on maximum switching frequency of 10 kHz at the base speed of 1500 RPM which results into Eq. 25. The total harmonic distortion (THD) calculated at

various speeds using the proposed quadratic function and the linear function is shown in Table 6. These results prove that the performance of proposed function in most of the cases is better than the linear function. In 5 out of 7 cases, the THD is lower in the case of the proposed carrier frequency operation. Moreover, the THD of the proposed method, in the 5 out of 7 cases, is almost half than the THD observed when the linear function is used. However, the THD is higher when the motor is running at 1200 RPM and 1500 RPM in the case of the proposed method e.g. at 1500 RPM the observed THD is 0.6 for the proposed method and 0.34 when the motor is operated with linear function.

$$f_c = 189 * (f_1) \tag{25}$$

Table 6: THD comparison of proposed and linear functions

Speed (RPM)	$f_c, linear$ (Hz)	THD (%)	$f_c, proposed$ (Hz)	THD (%)
200	1463.2	1.64	3242.5	1.37
500	3359.6	1.07	33748.5	0.66
800	5259.1	1.15	4867.1	0.51
1000	6524.2	0.57	5942.8	0.33
1200	7789.2	0.38	7289.2	0.54
1400	8600	0.91	8800	0.49
1500	9600	0.34	9800	0.6

3.8.2. Hybrid mode switching. The performance of the IFO drive system is tested for the hybrid mode switching above the base speed. The proposed hybrid mode switching scheme is also compared with the conventional mode switching scheme. The details of the test scenario used to compare the performance of both schemes is as follows. The motor is running at 1200 RPM and the inverter mode is SPWM. The reference is then changed from 1200 RPM to 1800 RPM. The inverter mode of operation should be switched from SPWM to the six-step mode during this speed transition.

The performance of the drive system when the conventional mode switching scheme is used is shown in Fig. 38 and Fig. 39. The oscillations in the motor speed are observed as shown in Fig. 38 (a), and the motor speed overshoots to 2188 RPM before settling to 1800 RPM. Moreover, the current also increases to approximately 2 A before settling back to the normal value. The Fig. 39 shows the speed (ω_r), current (i_a) and voltage (V_{ab}) as the mode is switched. The conversion from SPWM to square wave is visible in the voltage waveform plotted in Fig. 39 (b).

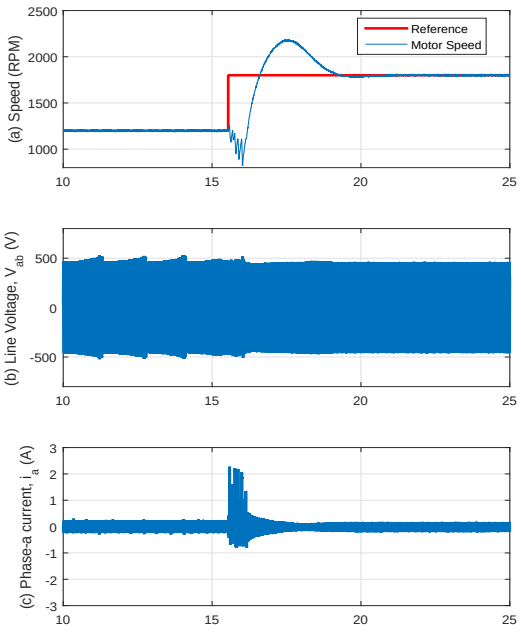

Figure 38: Mode switching (a) Speed (ω_r), RPM, (b) Line voltage (V_{ab}), V (c) Line current (i_a), A

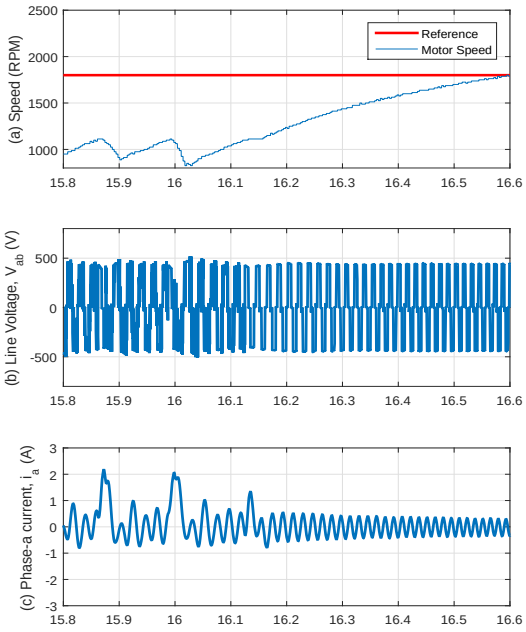

Figure 39: Mode switching (zoomed view) (a) Speed (ω_r), RPM, (b) Line voltage (V_{ab}), V (c) Line current (i_a), A

The hybrid mode switching operation is tested using the same test scenario mentioned above. When the speed changes from 1200 RPM to 1800 RPM, the six-step mode is invoked as shown in Fig. 40 and 41. The system remains stable as the motor speed changes from 1200 RPM to 1800 RPM as shown in Fig. 40 (a). Moreover, Fig. 41 (b) shows the voltage waveform at the time of the mode switching using hybrid PWM technique. Similar mode transition is visible for the line current (i_a) in Fig.41 (c). The line current (i_a) plotted here is obtained after filtering the measured current using a low

pass filter with a cut-off frequency of 100 Hz. When the mode is switched in Fig. 41, the voltage now is square wave. The mode switching happens because of the comparison of the square wave signal with the reference triangular signal which is now set to zero. Therefore, comparison of the reference signal with a triangular signal essentially transforms SPWM to square wave.

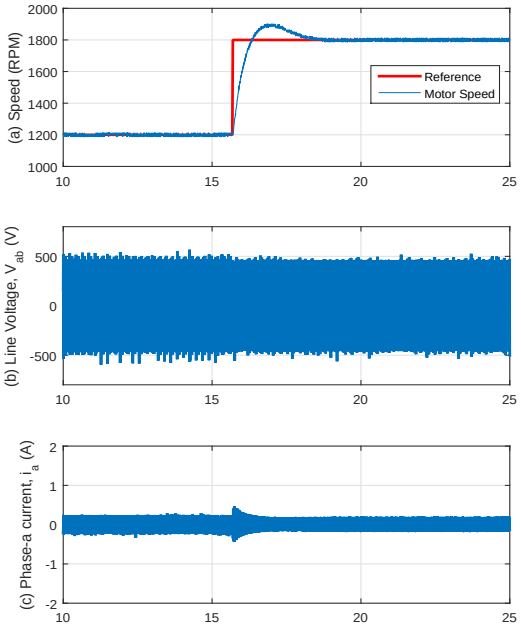

Figure 40: Hybrid mode switching (a) Speed (ω_r), RPM, (b) Line voltage (V_{ab}), V (c) Line current (i_a), A

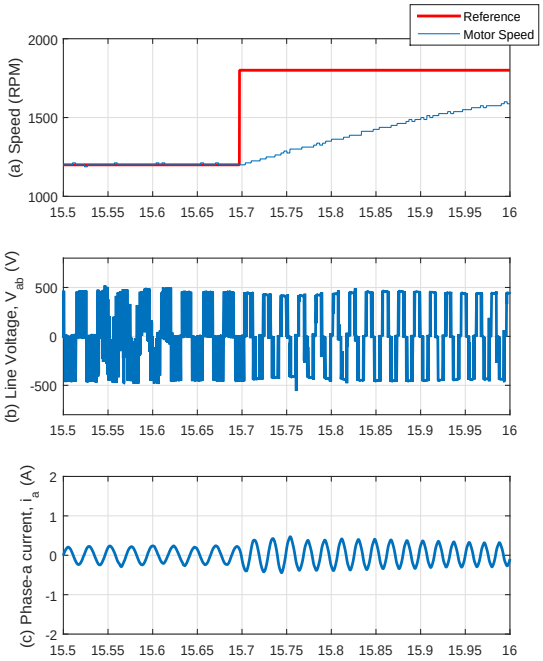

Figure 41: Hybrid mode switching (zoomed view) (a) Speed (ω_r), RPM, (b) Line voltage (V_{ab}), V (c) Line current (i_a), A

Chapter 4: Speed Regulator Design

Fractional order calculus is almost as old as the integer order calculus and its application to control systems is now well recognized. This chapter focuses on fractional calculus and fractional order proportional integral controllers (FO-PI). Several tuning rules exist in the literature that are optimized according to some criterion. The tuning rules selected for tuning of a PI controller and to be used in speed regulation of induction motors are presented and discussed in this chapter.

4.1. Integer Order PI/PID Controllers

The integer order PI controllers, as mentioned in the first chapter, are used in most of the industrial applications. An integer order PI controller is obtained by removing the derivative term from the PID controller given in Eq. 26, resulting in Eq. 27.

$$u(t) = K_p e(t) + K_i \int_0^t e(\tau)\, d\tau + K_d \frac{\mathrm{d}}{\mathrm{d}t}(e(t)) \tag{26}$$

$$u(t) = K_p e(t) + K_i \int_0^t e(\tau)\, d\tau \tag{27}$$

A large number of tuning rules exist for integer order proportional integral (PI) or proportional integer derivative (PID) controllers. The rules discussed in this work were developed in [32, 33]. These rules are mainly used for first order plus dead time (FPDT) model of the system. Eq. 28, 29 and 30 define the tuning rules presented in [32] and [33] respectively.

Ziegler-Nichols (ZN) tuning rules (28, 29) are probably the most widely used rules in the industry because of their simplicity and ease of implementation. These rules are simple and are based solely on the step response of the system, meaning, there is no need to obtain an exact model of the plant. In Eq. 28, X_o is the step reference command used to obtain the FPDT model as shown in Fig. 42 and K_o is used to calculate the proportional gain ($K_{p,zn}$). The integral gain ($K_{i,zn}$) follows from $T_{i,zn}$ and $K_{p,zn}$ as shown in Eq. (29).

$$K_o = \frac{X_o}{K_{proc}} \times \frac{T}{L} \tag{28}$$

$$\begin{aligned} K_{p,zn} &= 0.9K_o \\ T_{i,zn} &= 3.3L \\ K_{i,zn} &= \frac{K_{p,zn}}{T_i} \end{aligned} \tag{29}$$

Cohen-Coon (CC) tuning rules (30) are applicable to a class of plants with a relatively large dead time. The parameter 'R' is calculated from the dead time 'L' and time constant 'T' obtained from the open loop step response of the system. K_o used for determination of proportional gain '$K_{p,cc}$' is the same as defined in (28). The integral gain '$K_{i,cc}$' is calculated from 'L' and 'R' as follows.

$$\begin{aligned} R &= \frac{L}{T} \\ K_{p,cc} &= K_o\left(0.9 + \frac{R}{12}\right) \\ K_{i,cc} &= L\frac{(30+3R)}{9+20R} \end{aligned} \tag{30}$$

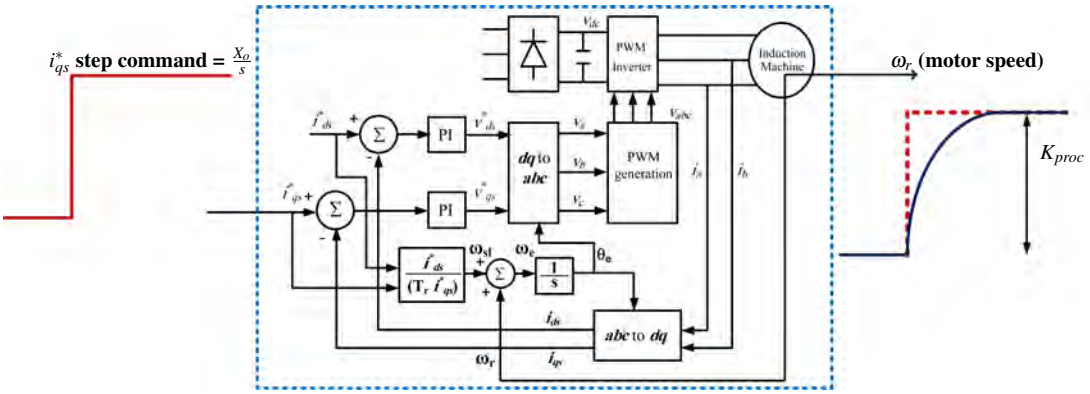

Figure 42: Plant step response

4.2. Fractional Order PID Controllers

The fractional order PID controller is obtained by replacing the integer order integrator and derivative with a fractional order integrator and derivative respectively as shown in Eq. 31. In this equation, K_{pf}, K_{df} and K_{if} are the proportional, integral and derivative gains of the fractional order PID controller. The fractional operator called as the differintegral operator $\left({}_{\alpha}\mathrm{D}_{t}^{\lambda}\right)$, is used for the evaluation of the integral of arbitrary order where α is the order of the integral and a and t are the terminals. Several definitions exist to evaluate the differintegral operator such as Caputo derivative, Riemann-Liouville (RL) or Grunwald Letnikov (GL) etc. The fractional order PI controller, in Eq. 32, follows from fractional order PID controller by removing the fractional derivative term from Eq. 31.

$$u(t) = K_{pf}e(t) + K_{if}\left({}_{\alpha}\mathrm{D}_{t}^{\lambda}e(t)\right) + K_{df}\left({}_{\alpha}\mathrm{D}_{t}^{\mu}e(t)\right) \tag{31}$$

$$u(t) = K_{pf}e(t) + K_{if}\left({}_{\alpha}\mathrm{D}_{t}^{\lambda}e(t)\right) \tag{32}$$

The fractional order Caputo derivative based implementation with a, t as the terminals as shown in Eq. 33 is used for the evaluation of the differintegral operator, ${}_{a}^{c}D_{t}^{\alpha}$. The differintegral operator can also be defined using the Grunwald Letnikov (GL) form, given in Eq. 34 or Riemann-Liouville (RL) form, given in Eq. 35 [54] but it is practically more useful to use Caputo derivative instead of *GL* or *RL* approximations.

$${}_{a}^{C}D_{t}^{\alpha}f(t) = \frac{1}{\Gamma(n-\alpha)}\int_{a}^{t}\frac{f^{(n)}(\tau)}{(t-\tau)^{\alpha+1-n}}d\tau \qquad (n-1<\alpha<n),(n\in\Re) \tag{33}$$

$${}_{a}\mathrm{D}_{t}^{p}f(t) = \lim_{\substack{t\to\alpha \\ nh=t-a}} h^{-p}\sum_{r=0}^{n}(-1)^{r}\binom{n}{r}f(t-rh) \tag{34}$$

$$ {}_{a}\mathrm{D}_{t}^{p} f(t) = \frac{1}{\Gamma(m+1-p)} \left(\frac{d}{dt}\right)^{m+1} \int_{a}^{t} (t-\tau)^{(m-p)} f(\tau) d\tau \tag{35} $$

The main advantages of the Caputo approximation are as follows. In the Grunwald-Letnikov (GL) form, the lower terminal 'a' is fixed while the memory length '(t-a)' is a function of 't' which becomes impractical when evaluating the differintegral for the initial conditions. The Riemann-Liouville (RL) integral is given in Eq. 35 where $(m \leq p \leq n), m = [p]$, and $[\cdot]$ represents the integer part of the argument (in this case, the integer part of p). The RL approach may lead to initial conditions which contain the limit values of the RL fractional derivative at the lower terminal $t = a$ [54, 55].

$$ \lim_{t \to \alpha} \left({}_{\alpha}D_{t}^{\alpha-1} f(t) \right) = b_1 \tag{36} $$

The fractional order PI controllers are known for their *Iso-damping* property. Iso-damping is the name given to the flat phase phenomenon displayed by the fractional order controllers. Having a flat phase response results in robustness against the plant gain variations. Therefore, while designing FO-PI controllers, the constant phase region is adjusted to be centered at the required operating frequency. The plot in Fig. 43 [55] is the gain and phase plot of an actual fractor with the order 0.8680. It shows the considerably flat phase response of a fractor, which is a device similar to a capacitor. This can be used to implement an analog fractional order integrator. The gain plot has slope which is not equal to 20 dB/decade.

4.3. Tuning Rules

There are several tuning rules reported in the literature developed for fractional order controllers. The tuning rules selected for this thesis were developed by Chen and Bhashkaran in [30]. These rules were developed using the *Fractional M_s constrained integral gain optimization (F-MIGO)* technique and are based on the first order plus dead time (FPDT) model (G_m) of the system represented in Eq. 37 where *'L'* is the dead time of the system, *'T'* is the time constant and K_{proc} is the *process gain*. The

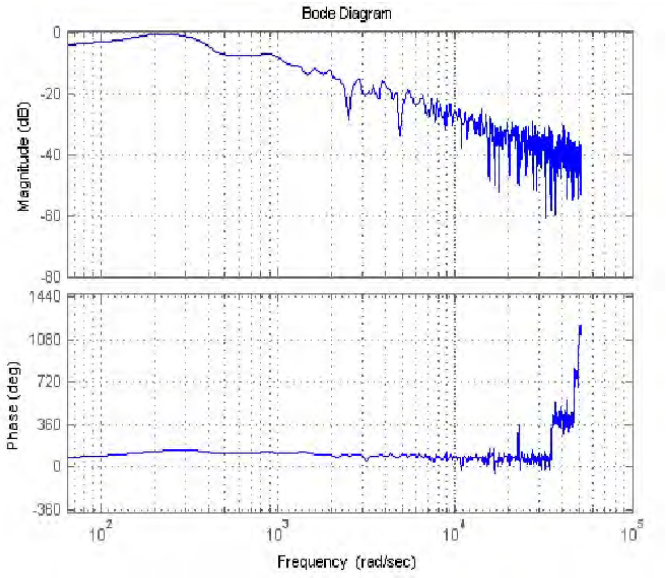

Figure 43: 'Fractor' bode plot, order(α) = 0.8680

tuning rules are represented by the expressions 38, 39, 40. In these equations, 'τ' is the *relative dead time* of the system and 'α' is the *order of the fractional integrator*. The parameter K^* is used as the proportional gain $K_{p,fo}$ and the integral gain ($K_{i,fo}$) is calculated from K^* & T^* (Eq. 41).

$$G_m(s) = \frac{K_{proc}e^{-Ls}}{Ts+1} \tag{37}$$

$$\tau = \frac{L}{T+L}, \alpha = \left\{ \begin{array}{ll} 1.1 & \tau \geq 0.6 \\ 1.0 & 0.4 \leq \tau \geq 0.6 \\ 0.9 & 0.1 \leq \tau \geq 0.4 \\ 0.7 & \tau < 0.1 \end{array} \right\} \tag{38}$$

$$K^* = \frac{1}{K_{proc}} \left(\frac{0.2978}{\tau + 0.000307} \right) \tag{39}$$

$$T_i^* = T \left(\frac{0.8578}{\tau^2 - 3.402\tau + 2.405} \right) \tag{40}$$

$$K_{p,fo} = K^*, K_{i,fo} = \frac{K^*}{T^*} \tag{41}$$

4.4. Performance Measures

The performance measures used for comparing different controllers are *integral squared error* (ISE), *integral absolute error* (IAE) and *integral time absolute error* (ITAE). These performance parameters are described by the expressions written in Eq. 42. IAE, ISE and ITAE provide a quantitative measure of a controllers' ability to force the error to zero. A lower value of these parameters show that the controller is able to achieve the required reference faster and with less effort.

$$\begin{aligned} IAE &= \int_0^t \|e(\tau)\| \, d\tau \\ ISE &= \int_0^t (e(\tau))^2 \, d\tau \\ ITAE &= \int_0^t t \cdot \|e(\tau)\| \, d\tau \end{aligned} \tag{42}$$

4.5. Design Methodology

The same test setup shown in Fig. 14 is used for the experimental evaluation of the proposed controller. The design methodology can be divided into the following steps:

1. Obtain the open loop step response of the current controlled induction motor
2. Obtain the FPDT model from the step response
3. Use the tuning rules for the integer order as well as the fractional order controllers to design both integer order and fractional order controllers

4.6. FPDT model of the system

It has been mentioned in chapter 2 that the speed control loop of an induction motor when operating under field oriented control, can be modeled as a first order plus dead time (FPDT) system. The FPDT model of the system is obtained from the S-shaped step response of the system.

4.6.1. Obtaining the FPDT model. The PID Tuner toolbox in MATLAB R14a is used to estimate the parameters of the transfer function from the step response data. The values of these parameters are obtained by feeding the step response shown in Fig. 44, to the PID Tuner toolbox in MATLAB R14a. The values of L, T and K_{proc} are found to be 0.03062s, 9.43s and 609.43 rad/sec respectively as shown in Eq. 43. The actual response in Fig. 44 matches the FPDT model response which shows that the approximate first order induction motor model is in-fact accurate. It is important to mention that the FPDT model should not be obtained through simulation, rather obtained experimentally because the actual test on the motor can take into account non-linearities as well as friction and actual inertia of the motor. Thus the FPDT model obtained experimentally in Eq. 43 is used for both simulation and experimental studies.

$$G_{ident}(s) = \frac{609.43}{9.43s+1} e^{-0.03062s} \tag{43}$$

4.6.2. Validation of FPDT model. After the model has been developed, the step response of the actual model and the approximate model is compared in Fig. 44. It can be seen that the response of the model obtained is very close to the actual motor response.

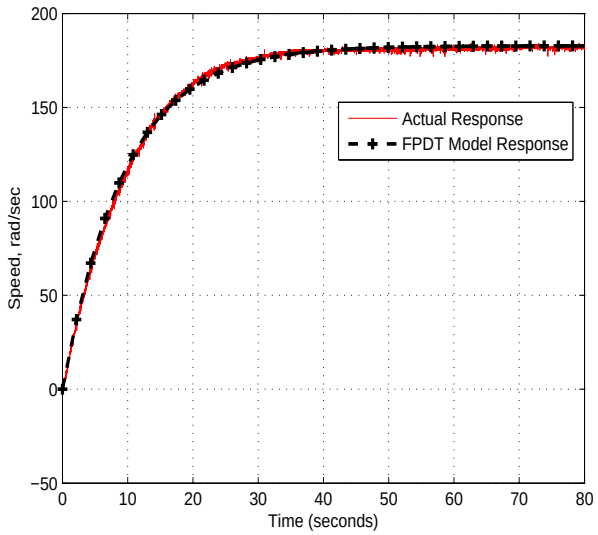

Figure 44: Step response of the system

4.7. Design of PI controllers

The design of the integer order PI controller and the fractional order PI controllers depends upon the time constant T, dead time L and the process gain K_{proc}. These parameters are obtained from the FPDT model developed in the previous section and is used to design both the integer order controllers and fractional order controllers.

The ZN-PI and CC-PI controller is designed by substituting the T, L and K_{proc} in Eqs. 28, 29 and 30 respectively. FO-PI controller is designed using Eq. 32. The corresponding K_p, K_i and α for the integer order and fractional order controller are tabulated in Table 7. Another integer order controller is designed using the trial and error technique (TE-PI) and the corresponding K_p and K_i are also tabulated in Table 7. Examination of the gains in this table shows that for the case of ZN-PI and CC-PI tuned controller the gains obtained are comparatively high as compared to the FO-PI controller which can potentially leads to the controller saturation and hence the performance of the system degrades. The design of the fractional order controller requires the determination of an additional parameter α which is the order of the integrator. For the proposed FO-PI controller, this order is found to be 0.7.

Table 7: PI controller gains

Parameters	FO-PI	ZN-PI	CC-PI	Trial & Error
α	0.7	1	1	1
K_p	0.1406	0.4647	0.4649	0.01
K_i	0.0407	4.5993	4.5853	0.02

4.8. Simulations Results

The simulations are performed using the integer order and fractional order controllers designed in the previous section and the results are compared using ISE, IAE and ITAE performance measures.

4.8.1. SIMULINK model. Using the simulation model of an indirect field oriented drive system developed in chapter 2, the PI controller used for speed control is modified to implement the fractional order PI controller. The block diagram constructed in SIMULINK is shown in Fig. 45 which is almost the same as the one used in Fig. 4 except the speed controller is replaced with either FO-PI controller or by any of the integer order controllers (i.e. ZN-PI, CC-PI or TE-PI).

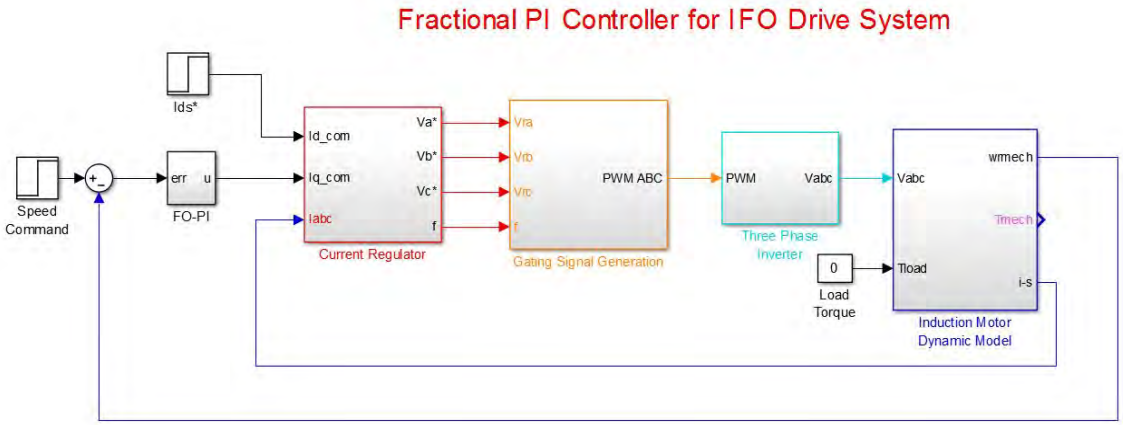

Figure 45: IFO drive system for FO-PI Controller

4.8.1.1. Implementation of fractional order controller. The fractional order integrator and differentiator can be estimated using continued fraction expansions and interpolation techniques (CFE), curve fitting or identification techniques [56] etc. The CFE techniques used in the literature are Carlson's method, Matsuda's method etc. and the curve fitting techniques are Oustaloup's method, Chareff's method etc. This work uses the Oustaloup's approximation of the differintegral operator which is defined by the transfer function ($H(s)$) shown in Eq. 44 where α is the order of the integral or differentiator and 'N' is the number of terms in the expansion. The constant ω_u is determined from the upper (ω_h) and lower (ω_h) bounds on the frequency. The value of ω_o and $\acute{\omega}_o$ is then calculated from the ω_u as shown in the Eq. 46. Similarly, the constants ω_k and $\acute{\omega}_k$ are determined from the Eq. 47. The Oustaloup's approximation is implemented in SIMULINK using the 'Ninteger' toolbox [57] as shown in the block diagram in Fig. 46 [57].

$$H(s) = C \prod_{k=-N}^{N} \frac{1+\frac{1}{\omega_k}}{1+\frac{1}{\acute{\omega}_k}} \tag{44}$$

$$\omega_u = \sqrt[2]{\omega_h \omega_b} \tag{45}$$

$$\begin{aligned} \omega_o &= \alpha^{0.5} \omega_u \\ \acute{\omega}_o &= \alpha^{-0.5} \omega_u \end{aligned} \tag{46}$$

$$\begin{aligned} \acute{\omega}_{k+1} &= \eta \omega_k \\ \omega_k &= \alpha \acute{\omega}_k \end{aligned} \tag{47}$$

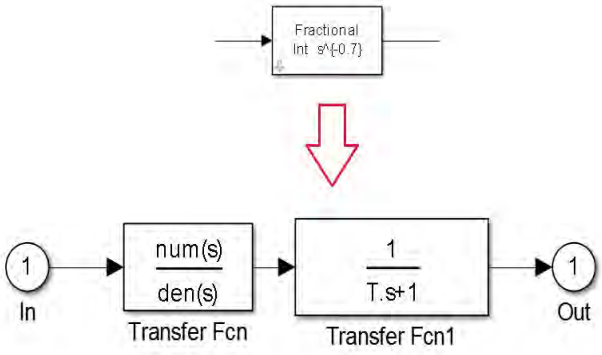

Figure 46: SIMULINK block using Oustaloup's approximation

4.8.2. Step response. In order to test the performance of all the controllers, the step command of 1400 RPM is set as reference and the corresponding step response is shown in Fig. 47. It can be seen from the plots that the CC-PI and ZN-PI controllers have the highest overshoot of 60.36% while the TE-PI controller has the overshoot of 16.42% i.e. lesser than both the CC-PI and ZN-PI controllers. The FO-PI controller has 5.7% overshoot which is lowest compared to all the other three controllers.

The results in terms of ISE, IAE and ITAE are plotted in the bar graph of Fig. 48. The IAE, ITAE, and ISE are the highest in the case of the trial and error tuned controller. This is because the induction motor takes a long time to settle to the reference that leads to high settling time. The other two integer order controllers i.e. ZN-PI and CC-PI controllers perform better than the trial and error controller. However, the FO-PI

controller outperforms all three integer order controllers (IO-PI). These results indicate that the FO-PI controller is promising for control of induction motors while requiring less tuning effort than other integer order controllers.

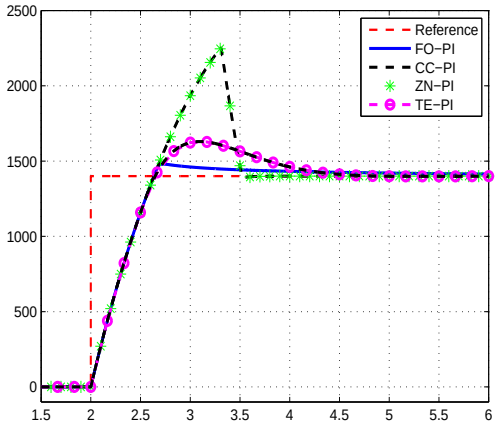

Figure 47: Step Response of all controllers

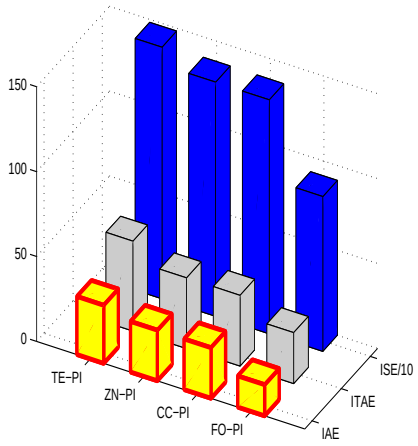

Figure 48: Performance of different controllers

4.8.3. Square wave tracking. The controller performance is tested for 1400 RPM square wave tracking. The simulation results under FO-PI and IO-PI (ZN-PI, CC-PI and TE-PI) controllers are shown in Figs. 49, 50. The controller parameters are kept the same as tabulated in Table 7 for all of the simulations and experimental study. The speed response of all the four controllers presented in Fig. 49 (a-d) shows that FO-PI controller has an overshoot of 8.3% which is less than three integer order controllers. The overshoot is highest in the case of CC-PI and ZN-PI controller i.e. 44.25%. The TE-PI controller, as shown in Fig. 49 (d), has an overshoot of 30.83% which is lower than CC-PI and ZN-PI controllers but higher than FO-PI controller.

It can be observed from Fig. 50 (b,c), that the CC-PI and ZN-PI controllers require the maximum allowable quadrature current (i_{qs}) for a longer period of time during the transient to track the same reference as compared to the FO-PI controller. The i_{qs} for TE-PI controller, plotted in Fig. 50 (d), shows that it requires lesser control effort than the CC-PI and ZN-PI controllers but its performance is poor as compared

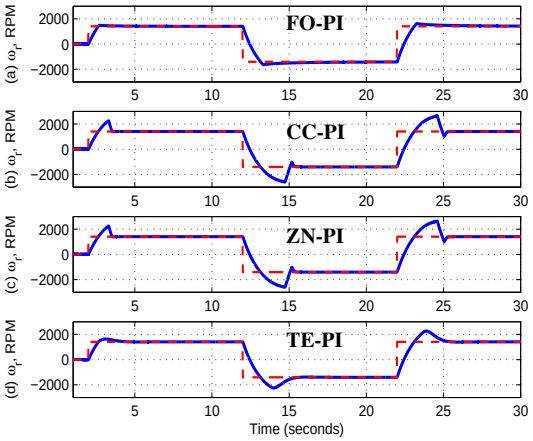

Figure 49: Simulation results for step response of FO-PI controller at 1400 RPM (a) FO-PI controller (b) CC-PI controller (c) ZN-PI controller (d) TE-PI controller

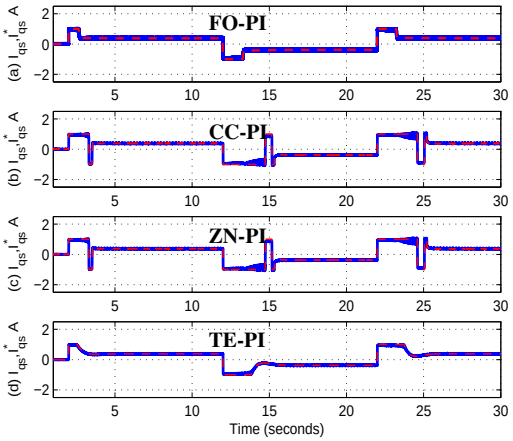

Figure 50: Control effort during square wave tracking at 1400 RPM (a) FO-PI controller (b) CC-PI controller (c) ZN-PI controller (d) TE-PI controller

to the FO-PI controller. The magnitude of i_{qs} in the case of both CC-PI and ZN-PI controllers is 1A for approximately 3.33 seconds, every time the reference changes. The FO-PI controller's i_{qs} is 1A for approximately 1.3 seconds. It can be concluded from these results that FO-PI controller designed using the tuning rules presented in section 4.3 result in lower overshoot while requiring lesser control effort as compared to integer order controllers (CC-PI, ZN-PI, TE-PI).

4.9. Experimental Results

The performance of the proposed speed controller is evaluated on the drive system represented by the block diagram Fig. 51 and developed using Lab Volt modules shown in Fig. 14. The controller gains are kept the same as tabulated in Table 7. The induction motor drive system is affected by the nonlinearities introduced due to the PWM based three phase inverter as well as the nonlinear nature of the motor itself. Three performance parameters, ISE, IAE, and ITAE as defined by Eq. 42 are used to compare these controllers' ability to accurately track the reference speed. Moreover, the control effort required by the controller to track the reference is used to evaluate the torque per amperes output of the machine. The currents plotted here are obtained after filtering using a low pass filter with a cut-off frequency of 100 Hz.

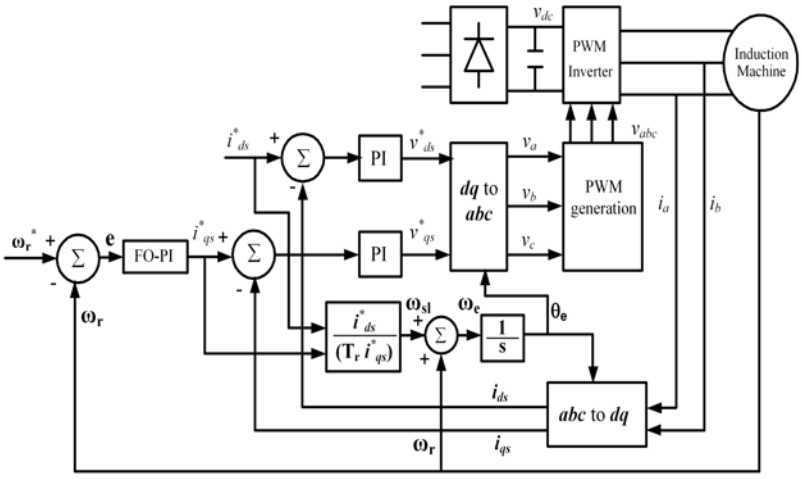

Figure 51: Fractional Order Proportional Integral based IFO drive system

4.9.1. Controllers' speed tracking performance evaluation. The speed tracking performance of the drive system is tested by setting a square wave of 1400 RPM as a reference. The step response of the drive system for all the four controllers is plotted in Fig. 52. The overshoot observed for the CC-PI and ZN-PI controllers is the highest as compared to all the other controlelrs. i.e. 53%. The overshoot is lowest in the case of FO-PI controller and the value is calculated to be 4.3%. The TE-PI controller has the overshoot of 14%. The observed percentage overshoot conforms to the ones observed in simulations.

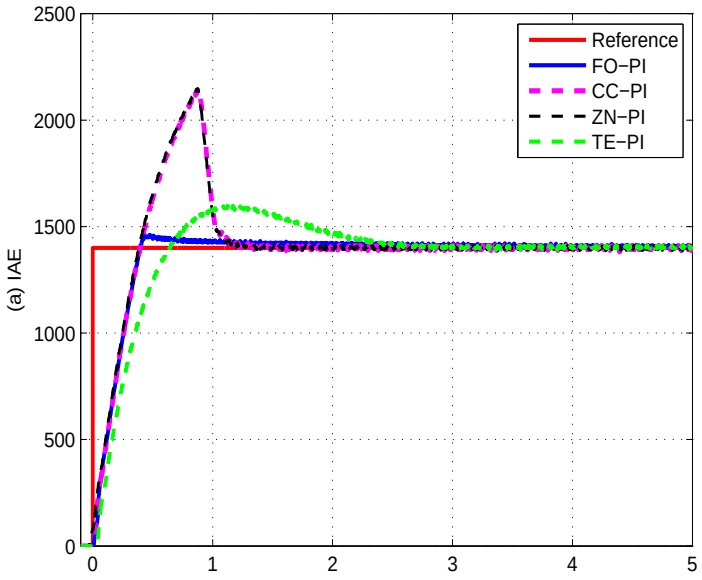

Figure 52: Experimental results of step response at 1400 RPM

The IAE, ISE and ITAE for the first 20 seconds, plotted in Fig. 53, shows that the FO-PI controller performs better than the integer order controllers. The IAE, ISE and ITAE at the end of 20 seconds is observed to be 38.75, 2494 and 1236 respectively when the motor speed is regulated by the FO-PI controller. The CC-PI and ZN-PI controllers performance is poor as compared to the FO-PI controller with IAE, ISE and ITAE of 67, 4574 and 2114 respectively for both controllers. This poor performance of the integer order controller is due to the high K_p and K_i gains. The TE-PI controller shows a slight improvement over the other integer order controllers and the IAE, ISE and ITAE observed are 59.32, 3258 and 1858 respectively.

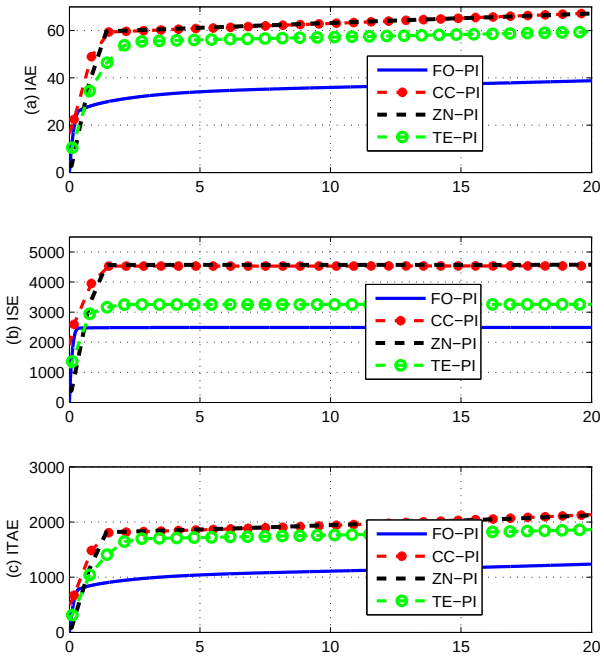

Figure 53: Comparison of step response performance of all controllers

The CC-PI and ZN-PI controller has an overshoot of 52.9 %, for the first step of 1400 RPM, which is considerably higher than the 4.07% overshoot for the FO-PI controller, thereby showing poor performance of CC-PI and ZN-PI controllers. The overshoot, when the TE-PI controller is used, is observed to be 10% which is comparatively lesser than the CC-PI and ZN-PI controllers. However, its performance is still worse than the FO-PI controller. The response of all four controllers for the square wave reference can be compared from Fig. 54 (a-d). As the reference changes from

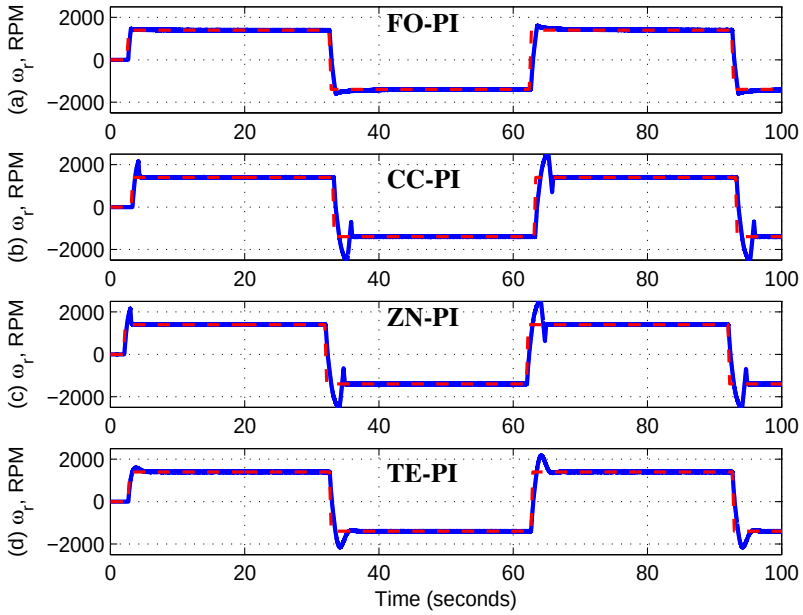

Figure 54: Experimental results of square wave tracking at 1400 RPM (a) FO-PI controller (b) CC-PI controller (c) ZN-PI controller (d) TE-PI controller

1400 to -1400 and vice versa, i.e. a step change of 2800 RPM, the percentage overshoot is observed to be 6.5% when FO-PI controller is used. The overshoot reduces to 41.78% for both CC-PI and ZN-PI controllers as compared to the overshoot when the reference changed from 0 to 1400 RPM. In the case of TE-PI controller, the overshoot increases to 27% when the reference changes from -1400 RPM to 1400 RPM compared to 10% overshoot observed when the reference changes from 0 to 1400 RPM.

The high K_p and K_i gains of CC-PI and ZN-PI controllers force the use of high control effort (i^*_{qs}) which runs the controller into saturation. The command i^*_{qs} and actual i_{qs} for all the four controllers are plotted in Fig. 55 (a-d). During the transient, all controllers apply maximum control effort (i^*_{qs}) to track the reference. However, during steady state, when the motor is running at 1400 RPM, the FO-PI controller output (i^*_{qs}) is limited between 0.09 and 0.3711 (only positive control effort). The control output of the CC-PI controller and ZN-PI controller (Fig. 55 (b,c)) constantly switches between 0.75 and -0.129 during steady state operation at 1400 RPM. Moreover, the mean of the absolute values of control effort (i^*_{qs}) observed in the case of the FO-PI controller is 0.2693 which is lesser than the absolute mean of the control effort (i^*_{qs}) observed in the case of the CC-PI and ZN-PI controllers i.e. 0.3731 and 0.3749 respectively. The

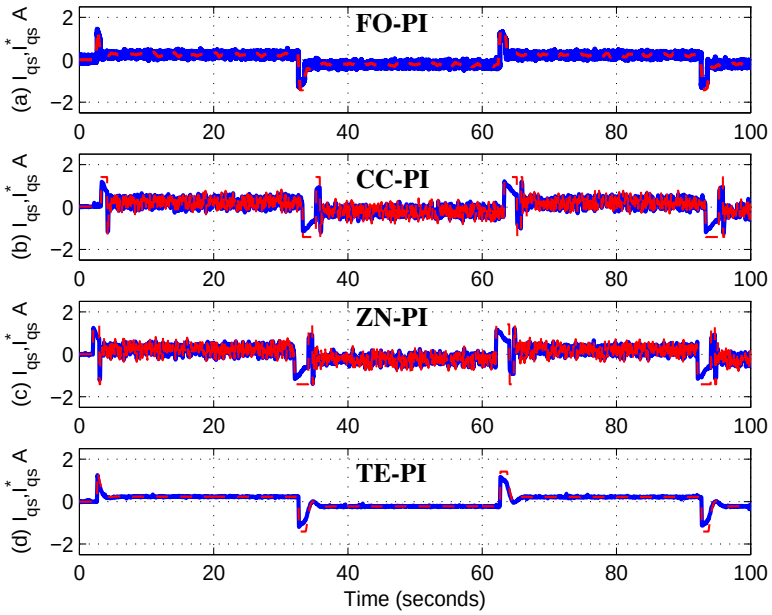

Figure 55: Control effort during square wave tracking at 1400 RPM (a) FO-PI controller (b) CC-PI controller (c) ZN-PI controller (d) TE-PI controller

absolute mean of the control effort (i^*_{qs}) in case of TE-PI controller is almost the same as the FO-PI controller i.e. 0.266 which shows that FO-PI and TE-PI have similar steady state characteristics. However, the lower control effort results in degradation of the transient performance of the TE-PI controller. This indicates that the designed FO-PI controller using the tuning rules presented above requires less control effort (i^*_{qs}) than its integer order counterparts (CC-PI and ZN-PI controllers) to track the same reference. Thus FO-PI can also maximize the torque per ampere output of the motor.

4.9.2. Low speed performance and disturbance rejection. In this section, the FO-PI controller performance is investigated for low speed tracking and disturbance rejection. A step command of 50 RPM is set for testing the low speed tracking. Figs. 56, 57 show the performance of FO-PI, CC-PI, ZN-PI and TE-PI controllers. All four controllers are able to track the reference; however, the CC-PI and ZN-PI controllers require more control effect (i^*_{qs}) as compared to the FO-PI controller. The absolute mean value of the control effort (i^*_{qs}) observed in the case of the FO-PI controller is 0.1859 which is again lower than the absolute mean value observed in the case of the CC-PI, ZN-PI and TE-PI controllers which are 0.3178, 0.3076 and 0.2953 respectively. Thus

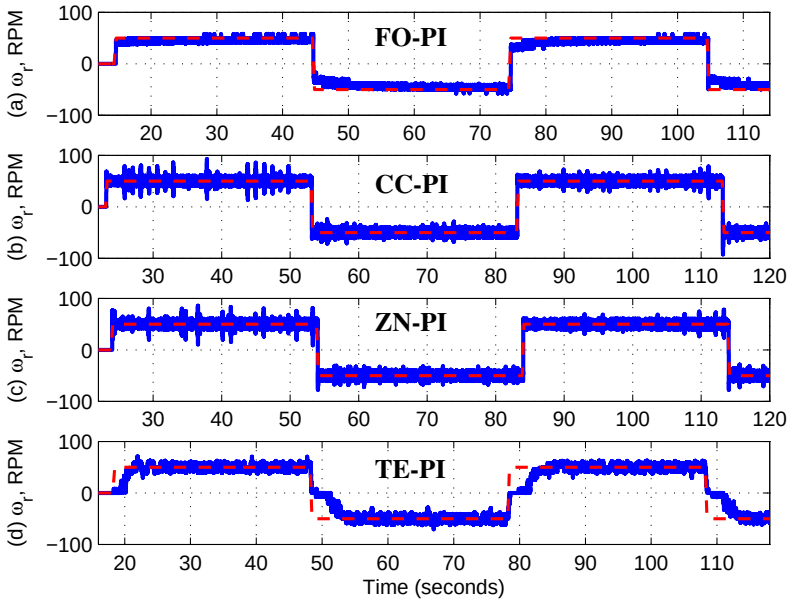

Figure 56: Experimental results of low speed square wave tracking at 50 RPM (a) FO-PI controller (b) CC-PI controller (c) ZN-PI controller (d) TE-PI controller

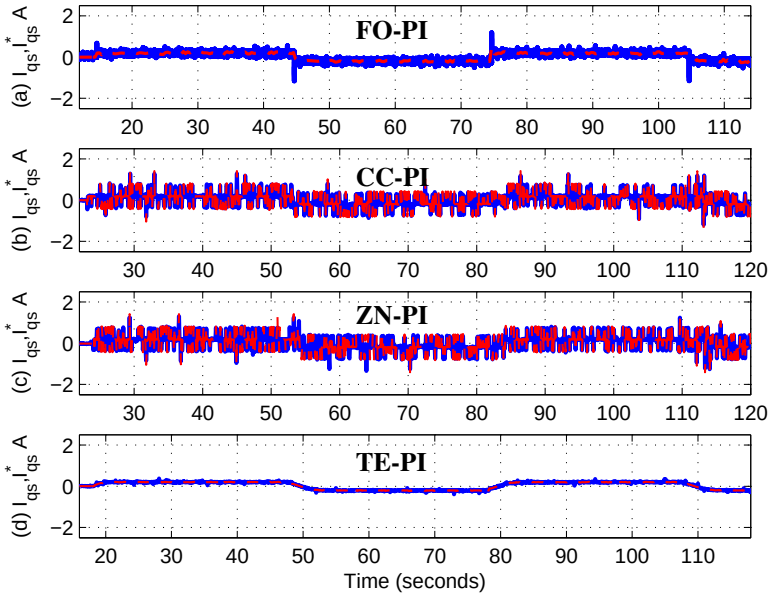

Figure 57: Control effort during square wave tracking at 50 RPM (a) FO-PI controller (b) CC-PI controller (c) ZN-PI controller (d) TE-PI controller

the FO-PI controller gives better torque per amperes compared to integral PI controllers. The controller tuned using trial and error is able to track the reference; however, the motor responds to the step command after a large delay time.

Next, the disturbance rejection of the controllers is evaluated by adding a step load at 20 seconds when the motor is running at 1400 RPM followed by removal of the load at 30 seconds. The speed response and i_{qs} are plotted in Figs. 58 and 59 respectively. The speed response of the FO-PI controller shows that the controller completely rejected the disturbance. The CC-PI and ZN-PI controllers also rejected the disturbance but by applying control input i^*_{qs} much higher than the FO-PI controller. The FO-PI controller applies an absolute mean control effort (i^*_{qs}) of 0.633 which is less than the control effort observed in the case of the other two controllers, i.e. 0.7338 and 0.7868 for CC-PI and ZN-PI controllers respectively. The trial and error tuned controller rejected the disturbance with almost the same control effort (0.635) as the FO-PI controller, as shown in Fig. 59, but the motor speed in case of TE-PI controller has a dip of about 200 RPM when the load is added and an overshoot of 200 RPM upon the removal of load. Thus the TE-PI controller is not able to effectively reject the disturbance.

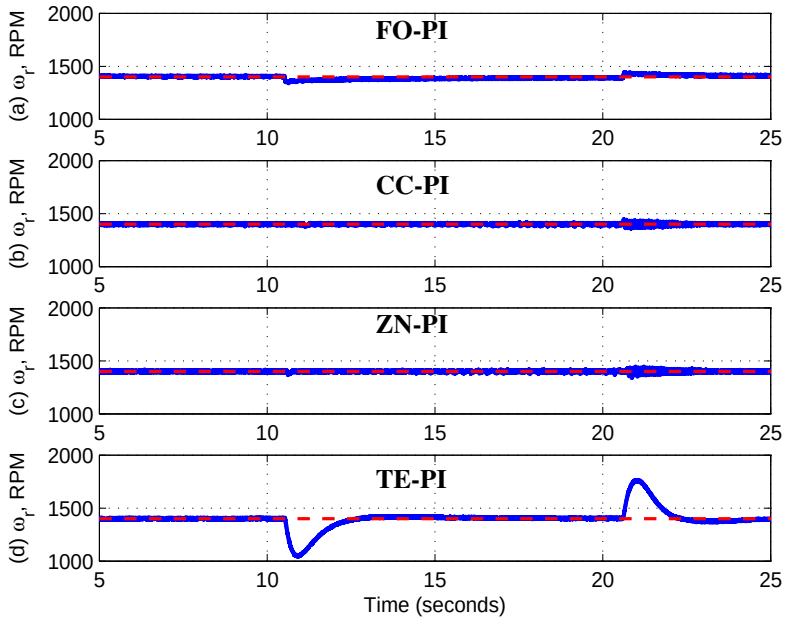

Figure 58: Experimental results of disturbance rejection at 1400 RPM (a) FO-PI controller (b) CC-PI controller (c) ZN-PI controller (d) TE-PI controller

4.9.3. Controller performance under detuning. The indirect field oriented control of an induction machine depends upon the feed forward slip calculation and

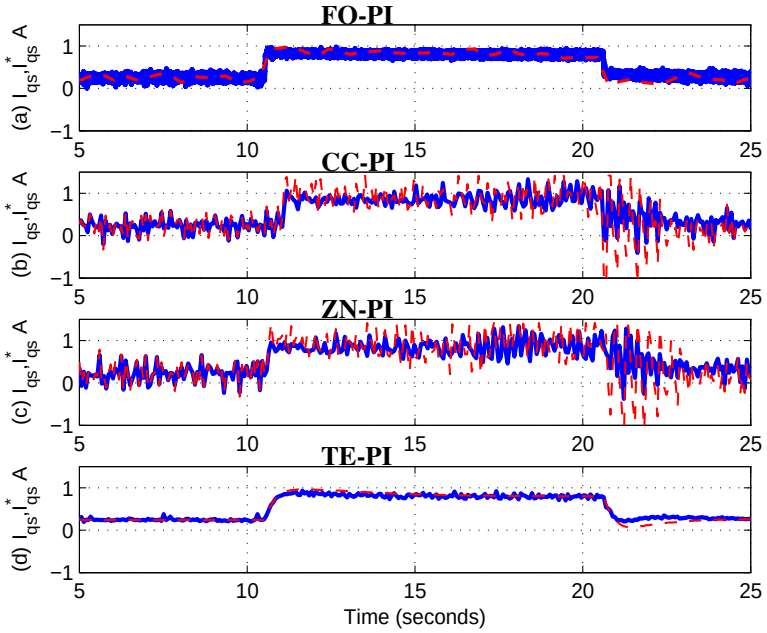

Figure 59: Control effort during disturbance rejection test at 1400 RPM (a) FO-PI controller (b) CC-PI controller (c) ZN-PI controller (d) TE-PI controller

the knowledge of accurate rotor time constant is critical. However, the heating and saturation effects can cause the motor parameters variation which results in detuning of the machine. This work evaluates the performance of FO-PI and PI controllers for a detuned machine. In order to test the controller performance under detuning, the reciprocal of rotor time constant ($\frac{1}{T_r}$) is changed as shown in Fig. 60 (a) while the motor is running at the constant speed of 1400 RPM and further loaded with 0.2 N.m torque. The speed tracking works very well as $\frac{1}{T_r}$ is doubled and further halved in the case of FO-PI controller. However, an overshoot of 20 RPM is observed as the $\frac{1}{T_r}$ is returned to its normal value at 58 seconds. The CC-PI and ZN-PI controllers maintain the speed but as the detuning persists, both controllers start to destabilize and lose tracking. A high overshoot is observed in the case of the TE-PI controller every time the $\frac{1}{T_r}$ is changed.

The current i_{qs}, plotted in Fig. 61, increases slightly to compensate for the detuning effects. In the steady state, and when the machine is detuned i.e. $\frac{1}{T_r}$ is set to 36, the i^*_{qs} varies between the maximum value of 0.53 and minimum value of 0.26 in the case of FO-PI controller. This range increases when the machine is controlled by the CC-PI and ZN-PI controller i.e. 1.03 and -0.147. The i^*_{qs} in the case of TE-PI controller varies between 0.44 and 0.41 which is lower than the other three controllers but at the

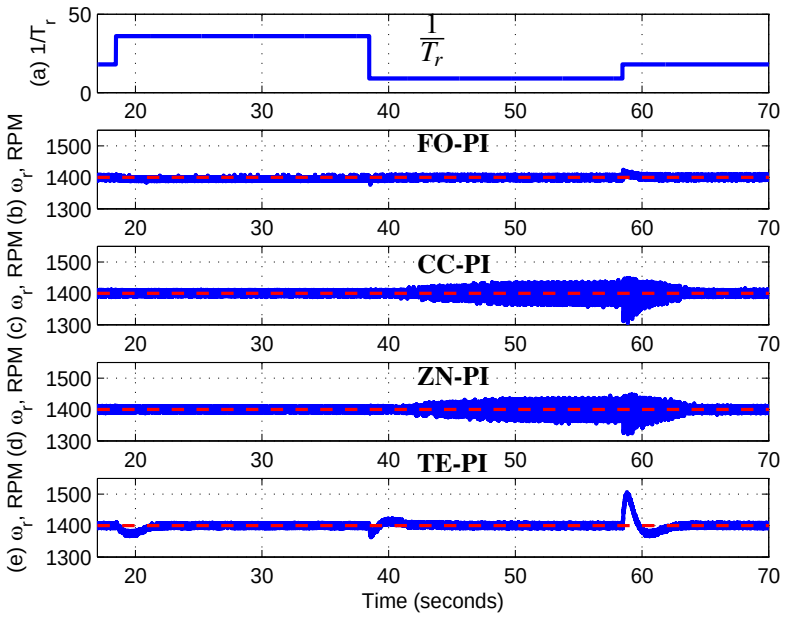

Figure 60: Experimental results of detuned machine operation at 1400 RPM (a) Rotor time constant $(\frac{1}{T_r})$ variation (b) FO-PI controller (c) CC-PI controller (d) ZN-PI controller (e) TE-PI controller

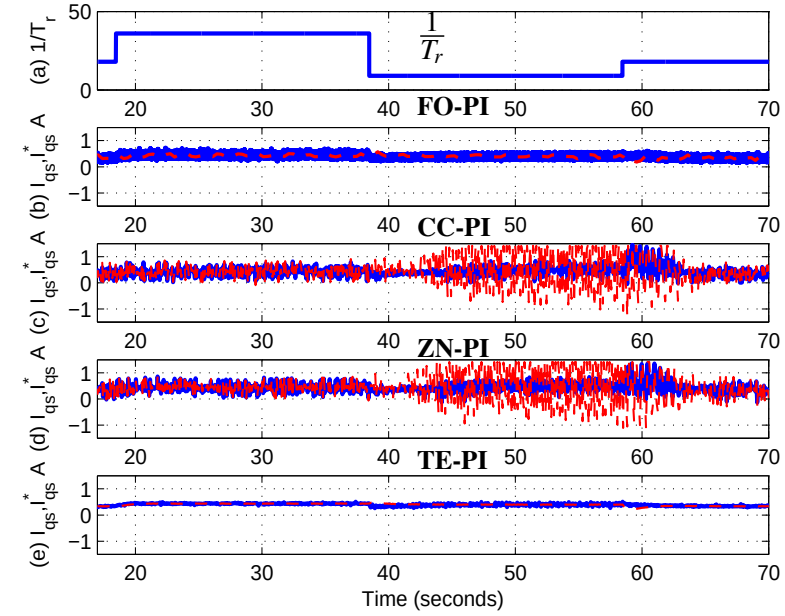

Figure 61: Control effort during detuned machine operation at 1400 RPM (a) Rotor time constant $(\frac{1}{T_r})$ variation (b) FO-PI controller (c) CC-PI controller (d) ZN-PI controller (e) TE-PI controller

expense of a high overshoot. Varying $\frac{1}{T_r}$ caused the CC-PI and ZN-PI controllers to destabilize and motor speed oscillates about the reference. Moreover, motor vibrations are also observed. These vibrations can be explained by the windup of the integrator because the controller was able to return to stable operation after some time as can be seen from Fig. 61 (c, d). The problem of windup is not observed when the motor is controlled using FO-PI or TE-PI controllers.

Chapter 5: Conclusion and Future Work

This thesis attempted to improve the performance of an indirect field oriented induction motor drive system by focusing on the optimum carrier frequency and PWM mode selection of the inverter and the controller design for motor speed regulation. Optimum carrier frequency selection reduced the harmonic and motor losses as well as the total harmonic distortion (THD). Moreover, the SPWM and square wave modes of operation are used in conjunction for high power and/or high speed applications. Thus a seamless mode transition technique has been proposed in this work by forcing the carrier frequency to zero for switching from square wave to SPWM and vice versa. The inverter operation is switched from SPWM to square wave mode when the speed increases above the base speed. The mode is switched back to SPWM when the speed decreases below the base speed by activating the carrier frequency.

A nonlinear FO-PI controller was the second major focus of this thesis. The designed FO-PI controller proved to perform better than the conventional integer order controllers. A first order plus dead time model of the induction motor is developed for the speed control of an IFO drive system, following which FO-PI and IO-PI (CC-PI, ZN-PI and TE-PI) controllers are designed. A quantitative comparison made using IAE, ISE and ITAE has shown that the FO-PI controller performs better as compared to ZN-PI, CC-PI, and TE-PI controllers. A high overshoot is observed in both simulation and experimentation when the drive system is tested for square wave tracking using the three integer order controllers. However, the FO-PI controller showed comparatively negligible overshoot in both simulation and experimentation. Also, the torque command current required by FO-PI controller showed that FO-PI controller provides better torque per amperes output of the machine as compared to linear PI controllers. The FO-PI controller further enhances the drive system performance with good disturbance rejection characteristics with minimal control effort as compared to the integer order controllers. The FO-PI controller also exhibited better speed tracking for a detuned IFO drive system while for ZN-PI and CC-PI controllers, not only the speed tracking became poor but also an unstable motor operation has been observed.

5.1. Summary

The major contributions of this research work can be summarized as follows:

1. A synchronous quadratic function for the PWM inverter is designed that synchronizes the carrier frequency with the fundamental frequency of the motor such that the motor losses and inverter switching losses are minimized through the entire speed range of the motor. The design of the proposed function is based on the analysis of the current at different carrier frequencies at different speeds to determine the optimum carrier frequencies.

2. A hybrid mode switching scheme is proposed that realizes seamless transition between the SPWM and six-step mode of operation by simply forcing the carrier frequency to zero. The proposed switching scheme ensures lower torque ripples and a smooth transition from SPWM to six-step mode and vice versa.

3. A nonlinear fractional order proportional integral (FO-PI) controller for speed regulation is designed. The proposed FO-PI controller has better disturbance rejection characteristics, lower overshoot and settling time, remains stable when the machine is detuned and works well at low speeds, as compared to the conventional integer order proportional integral controllers.

5.2. Future Work

One of the major suggested future work could be making the existing drive system sensorless. Speed estimation allows the removal of expensive rotary encoders. The speed sensor might not be practically feasible for some applications and it also makes the drive system expensive. Furthermore, another recommendation is to power the motor from a Lithium-ion battery bank and work on the energy management. This will make the drive system emulate the hybrid and electric vehicle traction system.

References

[1] C. D. Schauder, F. H. Choo, and M. T. Roberts, "High performance torque-controlled induction motor drives," *IEEE Trans. Ind. Appl.*, vol. IA-19, no. 3, pp. 349–355, May 1983.

[2] A. Eltom and A. Demirbas, "Motor system energy efficiency in the nylon industry: A comparison of PWM and square wave inverters," in *Proc. IEEE IEMDC, Miami, FL, USA*, May 2009, pp. 508–513.

[3] D. Diallo, M. E. H. Benbouzid, and A. Makouf, "A fault-tolerant control architecture for induction motor drives in automotive applications," *IEEE Trans. Veh. Technol.*, vol. 53, no. 6, pp. 1847–1855, 2004.

[4] N. Kar, K. Iyer, A. Labak *et al.*, "Courting and sparking: Wooing consumers? Interest in the EV market," *IEEE Electrific. Mag.*, vol. 1, no. 1, pp. 21–31, Sept. 2013.

[5] A. Shukla, "Fuelling future cars," *Journal of the Indian Institute of Science*, vol. 85, no. 2, p. 51, 2013.

[6] D. L. Greene and G. Duleep, "Status and prospects of the global automotive fuel cell industry and plans for deployment of fuel cell vehicles and hydrogen refueling infrastructure," *Oak Ridge National Laboratory, Oak Ridge*, 2013.

[7] H. Rehman and L. Xu, "Alternative energy vehicles drive system: Control, flux and torque estimation, and efficiency optimization," *IEEE Trans. Veh. Technol.*, vol. 60, no. 8, pp. 3625–3634, Oct 2011.

[8] F. Blaschke, "The principle of field orientation as applied to the new transvektor closed-loop control system for rotating field machines," *Siemens Rev.*, vol. 34, pp. 217–220, May 1972.

[9] N. Mohan, *Advanced Electric Drives:Analysis, Control and Modeling using MATLAB/SIMULINK*. John Wiley & Sons, 2014.

[10] R. Gabriel and W. Leonhard, "Field-oriented control of a standard ac motor using microprocessors," *IEEE Trans. Ind. Appl.*, vol. IA-16, no. 2, pp. 186–192, March 1980.

[11] R. Ueda, T. Sonoda, T. Matsuo *et al.*, "On sensing of flux and electromagnetic torque in air-gap of induction motor by means of hall effect in amorphous ribbon," in *Conf. Rec. of the 21st IEEE Ind. Appl. Soc. Ann. Meeting, Radisson Hotel, Denver, CO, USA, September 28-October 3, 1986*, vol. 1, p. 30.

[12] A. B. Plunkett, "Direct flux and torque regulation in a PWM inverter-induction motor drive," *IEEE Transactions on Industry Applications*, vol. IA-13, no. 2, pp. 139–146, March 1977.

[13] T. Lipo, "Flux sensing and control of static ac drives by the use of flux coils," *IEEE Trans. Magn.*, vol. 13, pp. 1403–1408, 1977.

[14] H. Rehman, "Design of voltage model flux observer," *Proc. Inst. Elect. Eng. - Elect. Power Appl.*, vol. 151, no. 2, pp. 129–134, 2004.

[15] H. Rehman, "Elimination of the stator resistance sensitivity and voltage sensor requirement problems for dfo control of an induction machine," *IEEE Trans. Ind. Electron.*, vol. 52, no. 1, pp. 263–269, 2005.

[16] H. Rehman, "A robust sensorless induction motor drive for alternative energy vehicular application," in *IEEE Int. Electric Vehicle Conf. (IEVC), Silicon Valley, CA, USA*. IEEE, 2013, pp. 1–5.

[17] M. Rodic and K. Jezernik, "Speed-sensorless sliding-mode torque control of an induction motor," *IEEE Trans. Ind. Electron.*, vol. 49, no. 1, pp. 87–95, Feb 2002.

[18] R. De Doncker and D. Novotny, "The universal field oriented controller," *IEEE Trans. Ind. Appl.*, vol. 30, no. 1, pp. 92–100, Jan 1994.

[19] W. Song, K. Smedley, and X. Feng, "One-cycle control of induction machine traction drive for high speed railway part II: Square wave modulation region," in *Proc. IEEE APEC, Fort Worth, TX, USA*, March 2011, pp. 1003–1009.

[20] K.-W. Lee, S. Park, and S. Jeong, "A seamless transition control of sensorless PMSM compressor drives for improving efficiency based on a dual-mode operation," *IEEE Trans. Power Electron*, vol. 30, no. 3, pp. 1446–1456, March 2015.

[21] R. Mahmood, T. Shah, and H. Rehman, "A hybrid PWM approach for the traction motor control of Alternative Energy Vehicles," in *Proc. IEEE Transportation Electrification Conference and Expo (ITEC), Dearborn, MI, USA*, June 2014, pp. 1–5.

[22] A. Ghaderi, M. Sugai, T. Umeno *et al.*, "A new direct torque control for AC motors with over modulation ability," in *IEEE Int. Electric Machines Drives Conference (IEMDC)*, May 2011, pp. 1247–1252.

[23] J. Holtz, "Pulsewidth modulation-a survey," in *Annu. IEEE Power Electronics Specialists Conference (PESC)*, Jun 1992, pp. 11–18 vol.1.

[24] S. K. Sahoo, T. Bhattacharya, and M. Aravind, "A synchronized sinusoidal pwm based rotor flux oriented controlled induction motor drive for traction application," in *Proc. IEEE APEC, Long Beach, CA, USA*, March 2013, pp. 797–804.

[25] J.-C. Hwang and H.-T. Wei, "The current harmonics elimination control strategy for six-leg three-phase permanent magnet synchronous motor drives," *IEEE Trans. Power Electron*, vol. 29, no. 6, pp. 3032–3040, June 2014.

[26] N. Oikonomou and J. Holtz, "Closed-loop control of medium-voltage drives operated with synchronous optimal pulsewidth modulation," *IEEE Trans. Ind. Appl.*, vol. 44, no. 1, pp. 115–123, Jan 2008.

[27] M. Aravind and T. Bhattacharya, "FPGA based synchronized sinusoidal pulse width modulation with smooth transition into overmodulation and six step modes of operation for three phase ac motor drives," in *IEEE Int. Conf. on Power Electronics, Drives and Energy Systems (PEDES)*, Dec 2012, pp. 1–6.

[28] V. Oleschuk, V. Ermuratskii, and V. Berzan, "Elimination of subharmonics in spectra of output voltage of drive inverters with space-vector PWM," in *IEEE Int. Conf. on Harmonics and Quality of Power (ICHQP), Bucharest, Romania*, May 2014, pp. 365–369.

[29] K. Fujisaki, M. Sakai, and S. Takeda, "Motor loss increment of induction motor driven by PWM inverter in comparison with inverter circuit loss," in *Int. Conf. on Electrical Machines and Systems (ICEMS), Sapporo, Japan*, Oct 2012, pp. 1–6.

[30] Y. Chen, T. Bhaskaran, and D. Xue, "Practical tuning rule development for fractional order proportional and integral controllers," *Journal of Computational and Nonlinear Dynamics*, vol. 3, no. 2, p. 021403, 2008.

[31] D. Xue, C. Zhao, and Y. Chen, "Fractional order pid control of a dc-motor with elastic shaft: a case study," in *Proceedings of American control conference*, vol. 7, 2006, pp. 3182–3187.

[32] J. G. Ziegler and N. B. Nichols, "Optimum settings for automatic controllers," *Trans. ASME*, vol. 64, no. 11, 1942.

[33] G. Cohen and G. Coon, "Theoretical consideration of retarded control," *Trans. ASME*, vol. 75, no. 1, pp. 827–834, 1953.

[34] J. Han, "From PID to Active Disturbance Rejection Control," *IEEE Trans. on Industrial Electron.*, vol. 56, no. 3, pp. 900–906, March 2009.

[35] J. Li, H.-P. Ren, and Y.-R. Zhong, "Robust speed control of induction motor drives using first-order auto-disturbance rejection controllers," *IEEE Trans. Ind. Appl.*, vol. 51, no. 1, pp. 712–720, Jan 2015.

[36] G. Feng, Y.-F. Liu, and L. Huang, "A new robust algorithm to improve the dynamic performance on the speed control of induction motor drive," *IEEE Trans. Power Electron*, vol. 19, no. 6, pp. 1614–1627, Nov 2004.

[37] A. Alexandridis, G. Konstantopoulos, and Q. Zhong, "Advanced integrated modeling and analysis for adjustable speed drives of induction motors operating with minimum losses," *IEEE Trans. Energy Convers.*, vol. 30, no. 3, pp. 1237–1246, Sept 2015.

[38] Z. Xu, J. Wang, and P. Wang, "Passivity-based control of induction motor based on Euler-Lagrange (EL) model with flexible damping," in *Int. Conf. Elect. Machines and Syst.*, Oct 2008, pp. 48–52.

[39] S. Chai, L. Wang, and E. Rogers, "A cascade MPC control structure for a PMSM with speed ripple minimization," *IEEE Trans. Industrial Electron.*, vol. 60, no. 8, pp. 2978–2987, Aug 2013.

[40] H. Liu and S. Li, "Speed control for PMSM servo system using predictive functional control and extended state observer," *IEEE Trans. Industrial Electron.*, vol. 59, no. 2, pp. 1171–1183, Feb 2012.

[41] E. Fuentes, D. Kalise, J. Rodriguez *et al.*, "Cascade-free predictive speed control for electrical drives," *IEEE Trans. Industrial Electron.*, vol. 61, no. 5, pp. 2176–2184, May 2014.

[42] P. Alkorta, O. Barambones, J. Cortajarena *et al.*, "Efficient multivariable generalized predictive control for sensorless induction motor drives," *IEEE Trans. Industrial Electron.*, vol. 61, no. 9, pp. 5126–5134, Sept 2014.

[43] V. Utkin, "Sliding mode control design principles and applications to electric drives," *IEEE Trans. Industrial Electron.*, vol. 40, no. 1, pp. 23–36, Feb 1993.

[44] X. Zhang, "Sensorless induction motor drive using indirect vector controller and sliding-mode observer for electric vehicles," *IEEE Trans. Veh. Technol.*, vol. 62, no. 7, pp. 3010–3018, Sept 2013.

[45] Y. Wang, Z. Wang, J. Yang *et al.*, "Speed regulation of induction motor using sliding mode control scheme," in *Conf. Rec. IEEE-IAS Annu. Meeting*, vol. 1, Oct 2005, pp. 72–76 Vol. 1.

[46] A. Saghafinia, H. W. Ping, M. Uddin *et al.*, "Adaptive fuzzy sliding-mode control into chattering-free IM drive," *IEEE Trans. Ind. Appl.*, vol. 51, no. 1, pp. 692–701, Jan 2015.

[47] B. Heber, L. Xu, and Y. Tang, "Fuzzy logic enhanced speed control of an indirect field-oriented induction machine drive," *IEEE Trans. Power Electron.*, vol. 12, no. 5, pp. 772–778, Sep 1997.

[48] M. Uddin, Z. R. Huang, and A. Hossain, "Development and implementation of a simplified self-tuned neuro fuzzy-based IM drive," *IEEE Trans. Ind. Appl.*, vol. 50, no. 1, pp. 51–59, Jan 2014.

[49] M. Masiala, B. Vafakhah, J. Salmon *et al.*, "Fuzzy self-tuning speed control of an indirect field-oriented control induction motor drive," *IEEE Trans. Ind. Appl.*, vol. 44, no. 6, pp. 1732–1740, Nov 2008.

[50] H. Michalska and D. Mayne, "Receding horizon control of nonlinear systems," in *Proc. 28th IEEE Conf. Decision Control*, Dec 1989, pp. 107–108 vol.1.

[51] P. C. Krause, O. Wasynczuk, S. D. Sudhoff *et al.*, *Analysis of electric machinery and drive systems*. John Wiley & Sons, 2013, vol. 75.

[52] T. Hägglund and K. J. Åström, "Revisiting the Ziegler-Nichols tuning rules for PI control," *Asian Journal of Control*, vol. 4, no. 4, pp. 364–380, 2002.

[53] M. H. Rashid, *Power electronics: circuits, devices, and applications*. Prentice hall NJ, 1988, vol. 2.

[54] I. Podlubny, *Fractional differential equations: An introduction to fractional derivatives, fractional differential equations, to methods of their solution and some of their applications*. Academic Press, 1998, vol. 198.

[55] S. Mukhopadhyay, "Fractional order modeling and control: Development of analog strategies for plasma position control of the STOR-1M Tokamak," MS thesis, Utah State University, USA, 2009.

[56] B. Vinagre, I. Podlubny, A. Hernandez *et al.*, "Some approximations of fractional order operators used in control theory and applications," *Fractional calculus and applied analysis*, vol. 3, no. 3, pp. 231–248, 2000.

[57] D. Valerio, "Ninteger v. 2.3 fractional control toolbox for matlab," 2005. [Online]. Available: https://www.mathworks.com/matlabcentral/fileexchange/8312-ninteger

Appendix-A Experimental set-up details

Table A1: Lab setup modules description

MOSFET inverter (LabVolt 8837)	
Maximum voltage	700 V
Maximum RMS current	1.5 A
Maximum peak current	3 A
Maximum switching frequency	20 KHz
Dynamometer (LabVolt 8960)	
Power rating	175 W
Load torque range	0 – 3 Nm
Power diodes (LabVolt 8842)	
Peak voltage	1200 V
Maximum current	1 A
Smoothing Inductors (LabVolt 8325)	
Inductance (used)	3.2 H
Maximum current	0.75 A
Hall effect current sensor (LEM LA-25 NP)	
Maximum primary current	25 A
Supply voltage	$\pm 15V$
Measuring resistor	220Ω

Appendix-B SIMULINK models

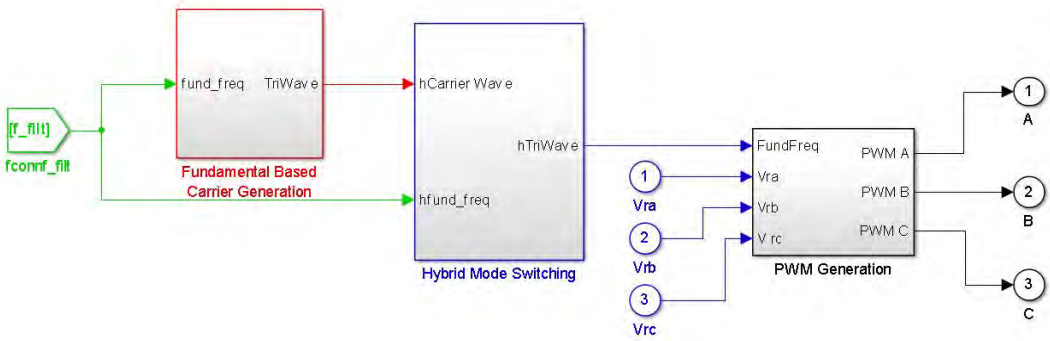

Figure B1: Block: 'Gating Signal Generation"

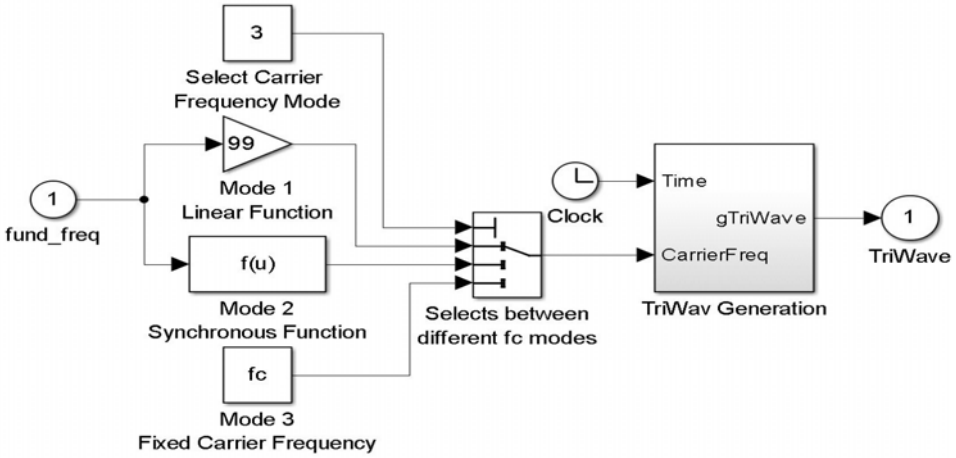

Figure B2: Block: 'Fundamental Based Carrier Generation'

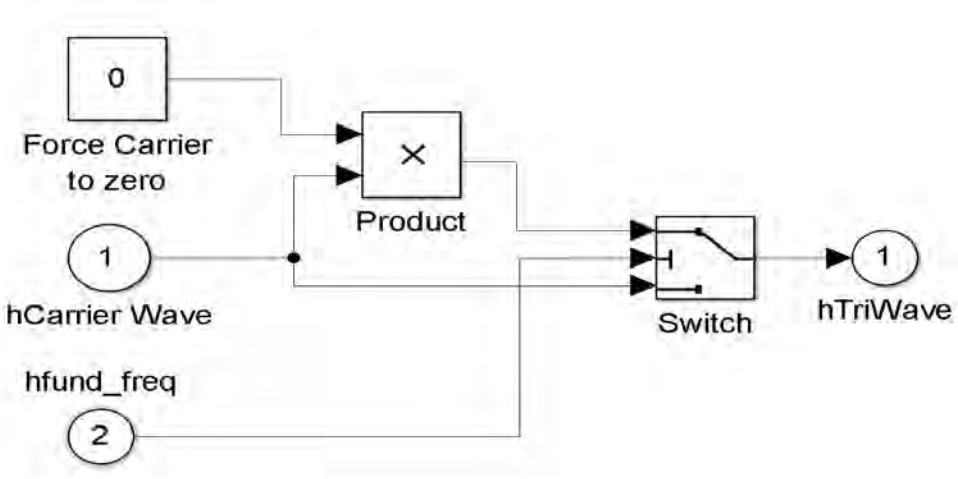

Figure B3: Block: 'Hybrid Mode Switching'

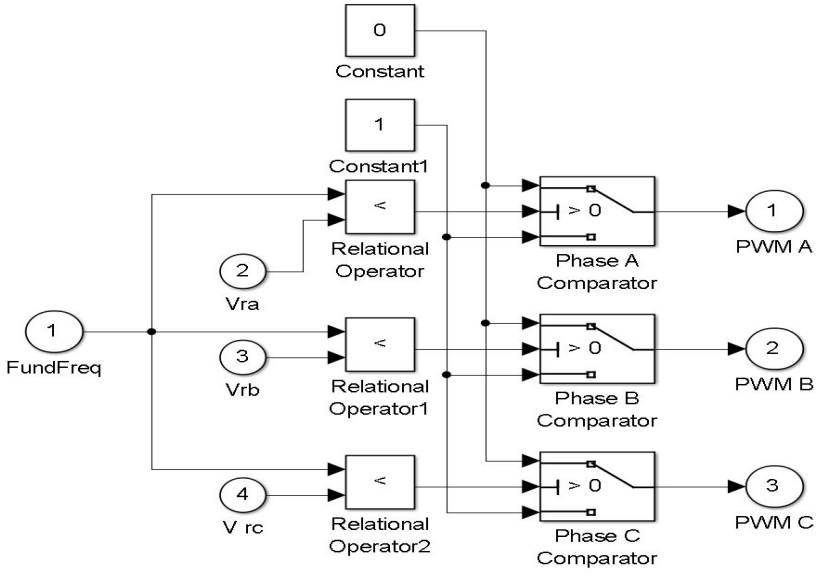

Figure B4: Block: 'PWM Generation'

Vita

Adil Khurram was born in 1991 in Karachi, Pakistan and grew up in Lahore, Pakistan where he completed his education from Cathedral High School, Lahore and Forman Christian College, Lahore. He graduated from National University of Science and Technology (NUST), Islamabad, Pakistan with a degree in Electrical Engineering. Adil joined u-blox in July 2013 where he worked on the development of 4G LTE protocol stack. He joined Masters program of Electrical Engineering in American University of Sharjah, UAE where he worked as a graduate research and teaching assistant from January 2014 - May, 2016. His research interests include field oriented AC drives and power electronics.